BAMS Article

# C-FOG

## Life of Coastal Fog

H. J. S. Fernando, I. Gultepe, C. Dorman, E. Pardyjak, Q. Wang, S. W Hoch, D. Richter, E. Creegan, S. Gaberšek, T. Bullock, C. Hocut, R. Chang, D. Alappattu, R. Dimitrova, D. Flagg, A. Grachev, R. Krishnamurthy, D. K. Singh, I. Lozovatsky, B. Nagare, A. Sharma, S. Wagh, C. Wainwright, M. Wroblewski, R. Yamaguchi, S. Bardoel, R. S. Coppersmith, N. Chisholm, E. Gonzalez, N. Gunawardena, O. Hyde, T. Morrison, A. Olson, A. Perelet, W. Perrie, S. Wang, and B. Wauer

**ABSTRACT:** C-FOG is a comprehensive bi-national project dealing with the formation, persistence, and dissipation (life cycle) of fog in coastal areas (coastal fog) controlled by land, marine, and atmospheric processes. Given its inherent complexity, coastal-fog literature has mainly focused on case studies, and there is a continuing need for research that integrates across processes (e.g., air–sea–land interactions, environmental flow, aerosol transport, and chemistry), dynamics (two-phase flow and turbulence), microphysics (nucleation, droplet characterization), and thermodynamics (heat transfer and phase changes) through field observations and modeling. Central to C-FOG was a field campaign in eastern Canada from 1 September to 8 October 2018, covering four land sites in Newfoundland and Nova Scotia and an adjacent coastal strip transected by the Research Vessel *Hugh R. Sharp*. An array of in situ, path-integrating, and remote sensing instruments gathered data across a swath of space–time scales relevant to fog life cycle. Satellite and reanalysis products, routine meteorological observations, numerical weather prediction model (WRF and COAMPS) outputs, large-eddy simulations, and phenomenological modeling underpin the interpretation of field observations in a multiscale and multiplatform framework that helps identify and remedy numerical model deficiencies. An overview of the C-FOG field campaign and some preliminary analysis/findings are presented in this paper.

**KEYWORDS**: Fog; Aerosols; Atmosphere-land interaction; Atmosphere-ocean interaction; Drop size distribution; Visibility

https://doi.org/10.1175/BAMS-D-19-0070.1
Corresponding author: Harindra J.S. Fernando, fernando.10@nd.edu
Supplemental material: https://doi.org/10.1175/BAMS-D-19-0070.2

In final form 10 August 2020

**AFFILIATIONS: Fernando, Richter, Dimitrova, Lozovatsky, Wagh, Wainwright, Bardoel, Coppersmith, Gonzalez, Hyde, and Wang**—University of Notre Dame, Notre Dame, Indiana; **Gultepe**—University of Notre Dame, Notre Dame, Indiana, and Environment and Climate Change Canada, Toronto, and University of Ontario Institute of Technology, Oshawa, Ontario, Canada; **Dorman**—Scripps Institution of Oceanography, University of California, San Diego, La Jolla, California; **Pardyjak and Hoch**—University of Utah, Salt Lake City, Utah; **Wang, Yamaguchi, Olson, and Wauer**—Naval Postgraduate School, Monterey, California; **Creegan**—Army Research Laboratory, White Sands Missile Range, New Mexico, and University of Notre Dame, Notre Dame, Indiana; **Gaberšek and Flagg**—Naval Research Laboratory, Monterey, California; **Bullock and Wroblewski**—Wood Environment and Infrastructure Solutions, St. Johns, Newfoundland, Canada; **Hocut**—Army Research Laboratory, White Sands Missile Range, New Mexico; **Chang, Nagare, and Chisholm**—Dalhousie University, Halifax, Nova Scotia, Canada; **Alappattu**—Moss Landing Marine Laboratory, Moss Landing, and Naval Postgraduate School, Monterey, California; **Grachev**—University of Notre Dame, Notre Dame, Indiana, and NOAA/Earth System Research Laboratories, and Cooperative Institute for Research in Environmental Sciences, University of Colorado Boulder, Boulder, Colorado; **Krishnamurthy**—University of Notre Dame, Notre Dame, Indiana, and Pacific Northwest National Laboratory, Richland, Washington; **Singh, Gunawardena, Morrison, and Perelet**—University of Utah, Salt Lake City, Utah; **Sharma**—University of Notre Dame, Notre Dame, Indiana, and University of Illinois at Urbana–Champaign, Urbana, Illinois; **Perrie**—Bedford Institute of Oceanography, Dartmouth, Nova Scotia, Canada

> "There it is, fog, atmospheric moisture still uncertain in destination, not quite weather and not altogether mood, yet partaking of both." —Hal Borland

Fog is a collection of suspended water droplets or ice crystals near the Earth's surface that causes horizontal near-surface visibility to drop below 1 km (Myers 1968; WMO 1992). Different from clouds, fog forms near the surface and hence dynamic, microphysical, physicochemical, thermodynamic, surface, and environmental processes that regulate moisture in the atmospheric boundary layer (ABL) undergird its formation, evolution (maturation), and dissipation, referred to as the *life cycle of fog* (Nakanishi 2000). The small diameter of fog droplets (~1–30 $\mu$m; Meyer et al. 1980) causes them to remain airborne by ambient turbulence for extended periods unless evaporated by heating, mixing with dry air, or coalescence to form drizzle (~50–100 $\mu$m; McGraw and Liu 2003). Societal impacts of fog are profound, for example, air, maritime, and ground transportation hazards due to low visibility; appearance of smoky fog (smog) in pollutant-trapped fog layers; and vast ecological consequences (as discussed by Torregrosa et al. 2014). In terrestrial optical communications, turbulence in fog-laden air causes beam scattering and irradiance fluctuations (i.e., scintillations; Mori and Marzano 2015; Fiorino et al. 2019). Gultepe et al. (2009) reckoned that economic losses due to fog are on par with winter storms, and Zhang et al. (2015) discussed fog-related operational challenges in the oil and gas industry. Although the topic is scientifically rich, has captivated top scientific minds (Taylor 1917; Jeffreys 1918; Ångström 1920; Bowen 1926), and our understanding has deepened over a century (Koračin et al. 2014; Dorman et al. 2017), fog prediction using numerical weather prediction models (NWP) remains a challenge (Wilkinson et al. 2013; Steeneveld et al. 2015; Román-Cascón et al. 2016). Factors underlying forecasting difficulties include an incomplete understanding and inherent multiscale and multiphase complexity of fog physics. Several comprehensive fog projects have been reported, for example, ParisFog (Haeffelin et al. 2010), FRAM (Gultepe et al. 2014), LANFEX (Price et al. 2018), Namibian Coastal fog (Spirig et al. 2019), WiFEX (Ghude et al. 2017), and European Action COST-722 involving 14 nations to improve short-term fog forecasts (Michaelides 2005).

Processes determining fog formation span from synoptic to microscales. The smallest flow scale in the ABL is ~1 mm (i.e., Kolmogorov scale) within which homogenization of temperature and gaseous water vapor occurs by viscous straining (Batchelor 1959), but spawning of water droplets occurs at still smaller scales surrounding hygroscopic fog condensation nuclei (FCN) (typically ~0.1 $\mu$m; Hudson 1980). This growth may originate at relative humidities (RH) as low as 33% (Torregrosa et al. 2014), but the growth rates become higher and droplets are sustained at higher RH (≥100%). Therefore, background conditions determining microphysical parameters such as the droplet number concentration ($N_c$), mean volume diameter (MVD), droplet effective radius ($r_e$), and liquid water content (LWC) are central to fog research. This underlies the rationale for regression-based fog forecasting tools based on NWP output statistics, synoptic conditions, and local geographic makeup, although these tools demonstrate limited success (Bergot 2013; Pu et al. 2016). Arguably, processes at meso-$\gamma$-scales (1–10 km) and microscales show stronger impact on fog genesis (Maronga and Bosveld 2017; Mazoyer et al. 2017). Thus, developing high-fidelity subgrid microphysical parameterizations for mesoscale NWP models is key to improving fog forecasts (Koračin et al. 2014).

Many classifications have been used for fog, among which three broad categories can be identified: radiation, advection, and mixing. Nocturnal radiative cooling of a moist air layer to or below its dewpoint leads to radiative fog. Advection of warmer air over colder water leads to warm fog (or cold fog, in the opposite case), and both are in the general category of advection fog. Mixing of nearly saturated warm and colder air masses produces mixing fog (Taylor 1917). Further identified within these are subcategories: steam fog (steam streaks/smoke arising within cold fog), precipitation fog (rain evaporating into drier air), ice fog (at air temperatures $T < -10$°C; Kim et al. 2014; Gultepe et al. 2015), and location-based types such as marine fog, valley fog, upslope fog, and land fog (Gultepe et al. 2016). Marine fog includes the categories of coastal fog (appearing in the coastal zone, the transition region between ocean and land where the influence of each other is felt), sea fog (appearing in shallower "green" water but away from the coastal zone, for example marginal seas and outer continental shelf), and the open-ocean fog (appearing in deeper "blue" water).

Coastal fog is the focus of this paper. It is one of the most challenging types, known for its sudden onset that defies predictability owing to three interacting and complex contributors: lower atmosphere, upper ocean, and land surface (O'Brien et al. 2013). Some noted coastal fog types include harr in eastern Scotland and England, fret in northeastern England, Labrador fog off eastern Canada, U.S. West Coast fog, and Yellow Sea fog. This paper presents a compendium of a 3-yr (2018–21) comprehensive research program dubbed C-FOG, designed toward better predictability of coastal fog via improved understanding of its life cycle, identifying deficiencies of forecasting models, and developing improved microphysical parameterizations. The project is centered on a field campaign surrounding the coasts of Avalon Peninsula, Newfoundland (NL), and Nova Scotia (NS), Canada, with measurements conducted simultaneously over land and aboard a research vessel (R/V). An extensive suite of in situ and remote sensing instruments was used, augmented by outputs of satellite and numerical modeling platforms. Validation of NWP models and identification of forecasting barriers were also emphasized. The expansiveness of the topic called for melding the expertise of a multidisciplinary team of researchers.

## Life cycle of coastal fog

***Formation.*** The formation mechanisms of coastal fog are diverse and lack unified classification. Literature review and C-FOG observations collectively allowed us to propose these categories of coastal-fog genesis:

(i) Advection of moist warm air over colder coastal waters. As an example, southerly wind flow over the warmer Gulf Stream and then over the colder coastal Labrador Current, which, upon cooling via air–sea exchange, produces a shallow *warm fog* in the Canadian Atlantic off Newfoundland (Isaac et al. 2020; e.g., Fig. 1).

(ii) Colder air moving over (evaporating) warmer ocean water to produce *cold fog*. Some examples are Arctic sea-smoke fog, which appears when frigid cold air passing over sea ice or frozen land reaches warmer coastal waters (Simei et al. 2001); advection of radiatively cooled air from land to warmer waters by land breeze (e.g., Yangtze River fog, Liu et al. 2016); and colder sea breeze traveling over a warmer coast (Gultepe et al. 2007).

(iii) Cyclones (low pressure systems) moving over coastal water, where Ekman pumping lifts moist air and forms low-level stratus clouds. Stratus base can be mixed downward by turbulence generated due to shear instabilities or cloud-top instability that occurs due to radiative cooling at the fog top (Deardorff 1980), thus forming fog (cf., Haeffelin et al. 2010). Reduction of sea surface temperature (SST) due to upwelled coastal water in response to cyclonic circulation may also help fog formation (Spirig et al. 2019; Lozovatsky et al. 2021).

(iv) Subsidence of (warming) air within an anticyclone (high pressure) over a cooler moist marine ABL generates a low-level inversion, leading to slowly descending stratus clouds. Cloud-top instability and turbulence mix and thicken the lowering stratus cloud base, which may envelop the surface as fog, for example, California coastal fog (Anderson 1931; Leipper 1948, 1994; Koračin et al. 2001).

(v) Near-saturated colder and warmer air masses mix by coastal turbulence episodes, thus generating *mixing fog* à la Taylor (1917). Some examples are the impingement of colder atmospheric gravity currents on coastal orography or instability of coastal jets.

***Persistence.*** The persistence of fog depends on factors such as the availability of moisture, irradiance, FCN, droplet characteristics, turbulence and mixing processes, advection, and environmental factors. Effective moisture supply mechanisms that help sustain fog include evaporation at the sea surface and moisture advection (Sverdrup 1942; Koračin et al. 2005). Intense radiative cooling at the fog-layer top and resulting turbulent convection beneath it mix the inversion associated with the fog top, and cool the fog layer beneath to maintain fog. Conversely, entrainment of dry air from above across the inversion under enhanced turbulence conditions lowers the humidity, impedes droplet growth, and hence reduces the longevity of fog layer. Entrainment at the fog top or a low-level stratus (with an interfacial buoyancy jump

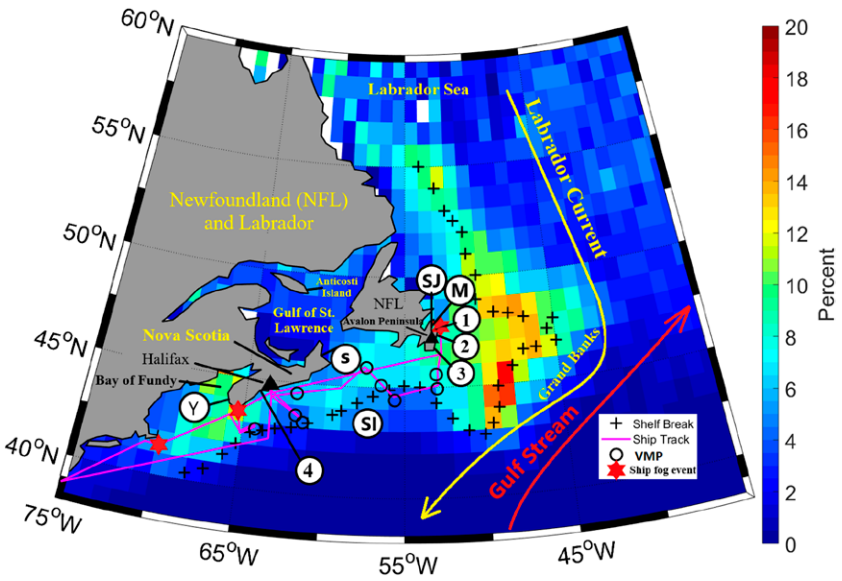


**Fig. 1. A map of North Canadian Atlantic overlaid by 1950–2007 fog climatology as a percentage of time of fog occurrence (color panel). Continental shelf break, major current systems, and prominent land and oceanic areas are shown. This is the region where C-FOG field campaign was conducted using an instrumented R/V and distributed land sites. R/V track, vertical microstructure profiler (VMP) casts, and fog events encountered by the ship are shown (see the text and inset). Campaign land sites: 1, Flatrock; 2, Blackhead; 3, Ferryland; and 4, Osborne Head. Routine sounding stations (M, Mount Pearl; Y, Yarmouth; and SI, Sable Island) and radar stations (Marble Mountain in western central NL; S, Marion Bridge near Sydney; SJ, Holyrood near St. John's and Halifax) used for forecasting are indicated. Black triangles are Halifax and St. John's ports.**

$\Delta b$) is determined by a stability parameter, either based on turbulent intensity $\sigma$ in the subcloud layer of height $h$ (bulk Richardson number $\mathrm{Ri}_b = \Delta b h/\sigma^2$) or the buoyancy frequency $N$ and squared vertical velocity shear $S^2 = \{(\partial U/\partial z)^2 + (\partial V/\partial z)^2\}$ across the inversion (gradient Richardson number $\mathrm{Ri}_g = N^2/S^2$; Fernando 1991). Note that $\mathrm{Ri}_b$ is a measure of subcloud (fog)-layer stability (stable when $\mathrm{Ri}_b \geq 1$) whereas $\mathrm{Ri}_g$ signifies inversion stability with $\mathrm{Ri}_g \leq 0.25$ favoring local turbulence production (Fernando and Hunt 1997).

***Dissipation.*** The dissipation of fog may occur when moisture supply is insufficient to maintain saturation conditions against evaporation, deposition, precipitation and scavenging (Leipper 1948). Therein, the near-surface layer first becomes slightly unsaturated, leaving stratus clouds aloft (sometimes called *lifted fog*). Another mechanism is the shear instability at the fog top ($\mathrm{Ri}_g \leq 0.25$), which enhances turbulent mixing and obliterates the cloud deck. The inward mixing mechanism proposed by Gurka (1978) occurs due to differential heating between the exterior and interior of fog patches. The dissipation in the periphery occurs first, the resulting outflow causes the fog layer to descend, followed by mixing of the entire layer upon $\mathrm{Ri}_b \leq 1$. Unfavorable transient weather (synoptic) conditions for fog maintenance may occur (Noonkester 1979; Koračin et al. 2005), thus promoting dissipation. An example is the fog dissipation on the Chinese coast of the Yellow Sea during synoptic wind shifts (Zhang et al. 2009; Li et al. 2012).

## C-FOG research program

A multidisciplinary group of researchers coordinated their expertise and resources to address a set of hypotheses on coastal fog (see sidebar). Specifically, the observational program addressed favorable large-scale to micrometeorological conditions; evolution of microphysical properties such as FCN, droplet characteristics, and their vertical profiles; radiative properties; heat,

## Coastal Fog (C-FOG) Research Program

The Coastal Fog (C-FOG) Research Program is a 3-yr (2018–21) effort funded by the Marine Meteorology Division of the Office of Naval Research (Code 322, ONR) with the following objectives: (i) improving our understanding of dynamical, microphysical, physicochemical, thermodynamic, terrestrial, and environmental processes underlying the life cycle of coastal fog; (ii) evaluating the efficacy of NWP models in fog prediction; and (iii) improving forecasting model skills. Comprehensive field measurements during 1 September to 8 October 2018 and research-grade LESs supported processes studies. NWP model investigations utilized COAMPS and WRF models. Owing to space–time variability and multiscale complexity, the *life cycle of coastal fog* remains enigmatic, and fog parameterizations used for NWP codes are largely empirical and leave much to be desired (Gultepe et al. 2017). Lack of rigorous treatment of surface processes, which causes biases in moisture and heat transports and energy budgets in models, is a contributor to the current low skill (~50%) of fog prediction (Pu et al. 2016). Specifically, the biases are pronounced at the marine–land–atmosphere interface, and addressing the underlying causes is a major task of C-FOG.

A number of hypotheses underpinned the design of field and numerical research programs: (i) Stability of the marine surface layer in warm fog conditions plays a critical role in fog life cycle as well as the strength (visibility), thickness, and longevity of fog. (ii) Convection during cold fog conditions leads to high space–time inhomogeneity (thermal plumes) and intense refractive index fluctuations in the fog layer, whereas rising plumes and their condensation lead to an overlying stratus deck. (iii) Under weak surface wind shear and turbulence conditions, low-level stratus clouds that overlie fog layers interact with the surface through convective motions induced by cloud-top instability and entrainment. (iv) Ocean–land–atmosphere interactions sensitively determine the nature and strength of coastal fog through processes such as sea/land breeze, coastal upwelling, SST variability, and orographic effects. (v) Turbulent intensity, wind speed, and microphysical and radiative properties of fog droplets set critical thresholds that demarcate different phases of fog evolution. Akin to these hypotheses was a set of science issues that are given in the text.

The main participating institutions include University of Notre Dame (UND, lead), Naval Postgraduate School (NPS), Moss Landing Marine Laboratory (MLML), Scripps Institution of Oceanography of the University of California, San Diego (Scripps), University of Utah (UU), and the Marine Meteorology Division of the U.S. Naval Research Laboratory, Monterey (NRL). Close collaborators were the U.S. Army Research Laboratory (ARL), Bedford Institute of Oceanography (BIO), Dalhousie University (DU), Department of National Defence, Canada (DND), Environment and Climate Change Canada (ECCC), National Center for Atmospheric Research (NCAR), University of Ontario Institute of Technology (UOIT), and Wood Environment and Infrastructure Solutions (Wood). The project supported a cadre of senior researchers, postdoctoral fellows, engineers, and graduate and undergraduate students.

momentum, water vapor, and surface energy fluxes and budgets; turbulence, entrainment, and mixing at the fog top; spatial inhomogeneity; optical turbulence and electromagnetic (EM) propagation; and the role of upper-ocean turbulence, in light of strong fog climatology observed over the continental break on some coasts (Dorman et al. 2021).

## Field campaign

The general locality of the campaign was selected based on Dorman et al. (2017), who pioneered global marine fog frequency analysis using (1950–2007) ICOADS (see Table 1 for

**Table 1. Selected acronyms.**

| | |
|---|---|
| ABL | Atmospheric boundary layer |
| AGL | Above ground level |
| CBH | Cloud-base height |
| CMC-HRDPS | Canadian Meteorological Centre High Resolution Deterministic Prediction System |
| COAMPS | Coupled Ocean–Atmosphere Mesoscale Prediction System |
| CVIS | Visibility Combined method |
| DUMBO | Dangling Ultrasonic Micrometeo Balloon-based Observations tethered system |
| EM | Electromagnetic |
| FCN | Fog condensation nuclei |
| FSL | (NOAA) Forecast Systems Laboratory algorithm |
| G2009 | Gultepe et al. (2009) algorithm |
| GFS | Global Forecast System |
| HRDPS | High Resolution Deterministic Prediction System |
| ICOADS | International Comprehensive Ocean–Atmosphere Dataset |
| IOP | Intensive operational period |
| LEMS | Local Energy Budget Measurement Station |
| LES | Large-eddy simulations |
| MSL | Above mean sea level |
| MWR | Microwave radiometer |
| MYNN2.5 | Mellor–Yamada–Nakanishi–Niino (level 2.5) |
| NASU | Naval Postgraduate School (NPS) Aerosol Sampling Unit |
| NAM | North American Mesoscale Forecast System |
| NAVGEM | (U.S.) Navy Global Environmental Model |
| NL | Newfoundland |
| NS | Nova Scotia |
| NSSL | National Severe Strom Laboratory |
| NWP | Numerical weather prediction |
| PBL | Planetary boundary layer |
| PWD | Present weather detector |
| RAP | Rapid Refresh weather forecast model |
| Rapid RUC | Rapid Update Cycle weather forecast model |
| SIOP | Ship intensive operational period |
| SST | Sea surface temperature |
| SW99 | Stoelinga and Warner (1999) algorithm |
| TKE | Turbulent kinetic energy |
| TLS | Tethered lifting system |
| YSU PBL | Yonsei University (YSU) PBL scheme |
| WRF | Weather Research and Forecasting Model |
| WRF-ARW | Advanced Research WRF |

acronyms) weather observations (Fig. 1). Accordingly, significantly greater global marine fog occurrences are concentrated in 12 maxima, two of which are off eastern Canada along the NS and NL coasts, which represent inversion-capped fog during the warm season belonging to rising/lowering stratus. Another option was the U.S. West Coast, which is rich in coastal fog. Considering competing factors, coasts of NS and NL were selected for C-FOG because of logistical reasons and they are underrepresented in the literature. During a scouting trip from 28 to 30 May 2018, four study sites were identified: Ferryland, Blackhead, and Flatrock, all on private land in NL, and Osborne Head, a property of Department of National Defence (DND) in NS (see sidebar).

Although the densest eastern Canadian fog climatology is during July and August, the campaign was from 1 September to 6 October 2018 due to the possibility of overlapping fog events in July and August, which preclude the capture of most distinctive differences between various phases of events. The land instrument deployment started on 14 August, with data acquisition immediately following each installation, and teardown started on 8 October. The instrumented R/V *Hugh R. Sharp* departed from Lewis, Delaware, on 31 August and returned on 8 October, with three port calls (for ship tracks, see Fig. 1).

Each location's instrumentation is shown in Figs. 2a–d and Fig. ES1 in the supplemental material. The descriptions of the instruments/platforms at all sites are given in Tables 2–8, which are expanded in Tables ES1–ES7 to include their technical specifications. All sites housed multiple video cameras, providing a continuous record of visual observations.

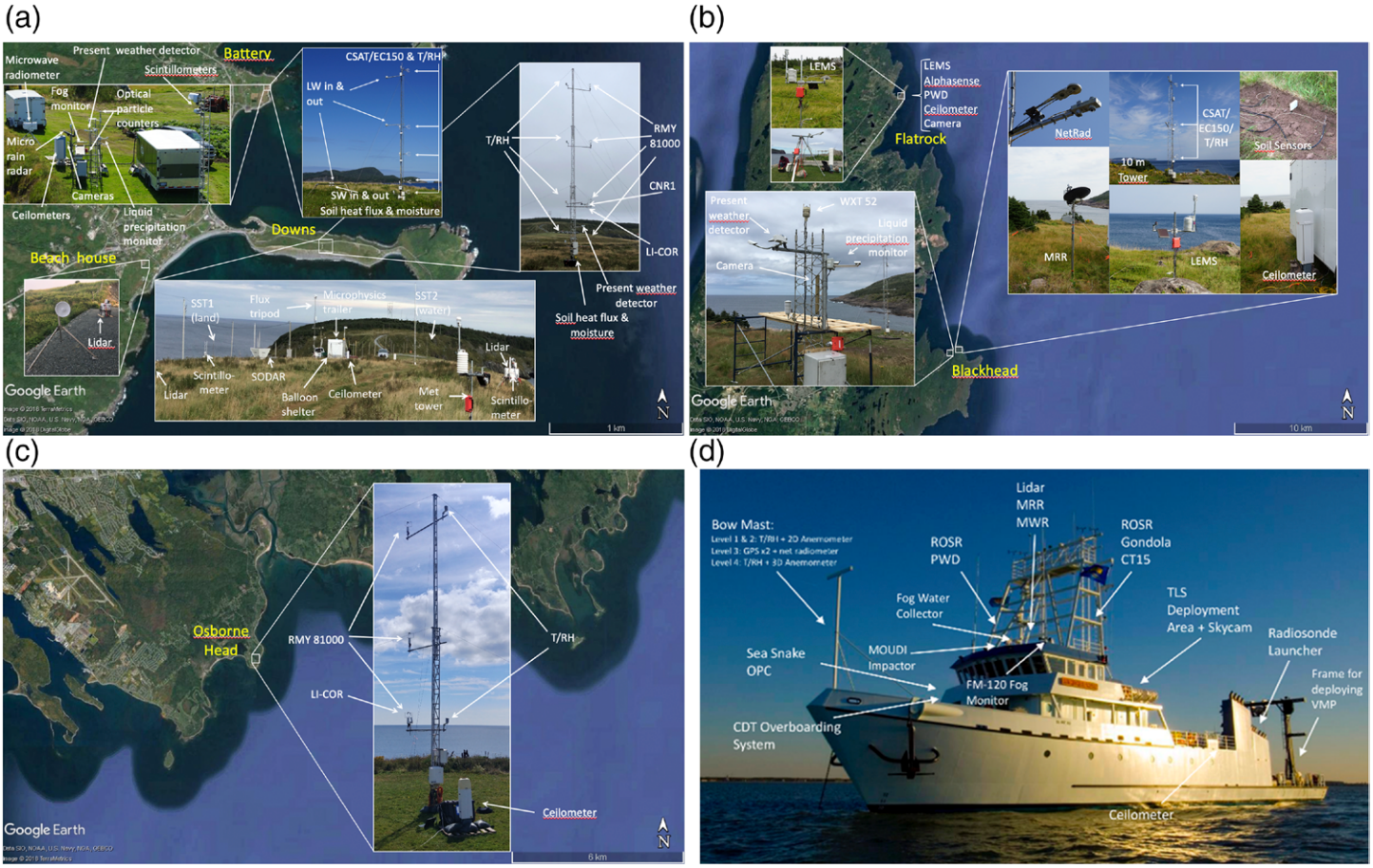


**Fig. 2. Photographs of land sites and R/V with instrumentation. (a) Ferryland sites: Downs, Battery, and Beach House (Judges Hill is in Fig. ES1); (b) Flatrock and Blackhead sites; (c) Osborne Head site; and (d) R/V *Hugh R. Sharp*. Details of instrumentation are given in the text. SST1 and SST2 are the IR pyrometers for land and water surface temperature measurements. Additional photographs are in Fig. ES1.**

**Table 2. Measurement instruments deployed during C-FOG for Downs site.**

| Instrument or instrument system/platform | Measured or retrieved parameters |
|---|---|
| Two Halo Photonics Streamline$^{XR}$ Doppler lidars, dual-Doppler scanning configuration | Profiles of wind speed and turbulence (horizontal and vertical) |
| Two MFAS Sodar-RASS systems, separated by 200 m | Wind and temperature profiling |
| Vaisala CL31 ceilometer | Cloud-/fog-base height and aerosol backscattering, three cloud layers |
| Two Scintec BLS900 near-infrared Scintillometer transmitters. Receivers at Beach House and Battery sites 1.444 km to Battery, ~1.3 km to Beach House | Path-averaged turbulence $C_n^2$ and $C_T^2$, sensible heat flux, transmitted energy, $V_R$, transmitted wavelength: 0.880 $\mu$m |
| Radiometer Physics GmbH microwave MWS-160 Scintillometer, receiver; MWS-160 is collocated with BLS 900, transmitter at Battery | Path-averaged turbulence ($C_n^2$ and $C_q^2$), latent heat flux, transmitted energy, $V_R$, transmitted wavelength: 1860 $\mu$m |
| Vaisala RS41-SGP Radiosonde Launcher and Vaisala DigiCORA Sounding System MW41 | Meteorological profiles of *P*, *T*, RH, wind speed (WSpd), and wind direction (WDir) |
| Flux Tower (16.2 m): four levels of R.M. Young (Model 81000) 3D sonics and Rotronic HC2-S3 *T*/RH (2, 5, 10, and 15 m AGL); LI-COR LI-7500A Open Path $H_2O/CO_2$ Gas Analyzer at 5 m AGL; Kipp and Zonen (K&Z) CNR1; Vaisala PWD22 present weather detector; Campbell Scientific Inc. (CSI) CS616 probe, CSI CS109 buried soil thermistor and Hukseflux HFP01 heat flux plate all buried −5 cm near the flux tower | Sonics for three components of wind velocities, turbulence, sonic *T*; HC2-S3 for *T* and RH; LI-COR for water vapor and $CO_2$ turbulent fluxes; CNR1 for up- and downwelling short- and longwave radiation; PWD 22 for visibility and precipitation; CS616 for soil moisture (volumetric water content); CS109 for soil T; HFP01 for soil heat flux |
| Tripod mast (6 m): Campbell Scientific IRGASON—Integrated $CO_2$ and $H_2O$ open-path gas analyzer at 5.9 m and 3D Sonic Anemometer; three levels of Vaisala HMP155 and WXT520 (1.5, 2.2, and 5.9 m); Kipp and Zonen CNR1 net radiometer at 3.2 m; CSI SS109 buried thermistor (−0.6 and −6 cm); CSI CCFC field camera | IRGASON for $CO_2$ and $H_2O$ concentrations, 3D wind velocity, sonic *T*, bulk *T* and *P*, turbulent fluxes of momentum, sensible and latent heat; HMP 155 for mean *T*, RH; WXT 520 for mean wind, *P*, *T*, RH; CNR1 for up- and downwelling shortwave and far infrared radiation; SS109 for soil *T* |
| NPS Aerosol Sampling Unit (NASU) Microphysics Trailer: located 21 m from the tripod: TSI 3010 condensation particle counter (CPC); Droplet Measurement Technology (DMT) CDP-2; Radiance Research PSAP; Brechtel TAP soot photometers; TSI 3563 Integrating Nephelometer | TSI 3010 for aerosol total number concentration; CDP-2 for cloud/fog droplet size spectrum; PSAP for aerosol absorption; TAP for aerosol absorption; TSI 3563 for aerosol scattering |
| Dangling Ultrasonic Micrometeo Balloon-based Observations (DUMBO) tethered system, a 32 $m^3$ Allsopp Helikite balloon platform: CSI IRGASON, VectorNav VN100 IMU, Rotronic HC2-S3 *T*/RH; CSI CR6 data acquisition system; Anasphere SmartTether v8 tethersonde system | IRGASON: as above; VN100 for inertial motion unit, linear acceleration, rotation rates, attitude angles; HC2-S3L for *T* and RH; SmartTether v8: mean wind, *P*, *T*, RH. |
| Local Energy Budget Measurement Station (LEMS): Meter Environment Atmos 22 2D sonic anemometer; Sensirion SHT31 air *T*/RH probe; Decagon 5 TM soil temperature and moisture sensors; Melexis MLX90614 surface *T* sensor; LI-COR Li200R global radiation sensors; Bosch BMP280 pressure sensor | Autonomous, solar-powered, Arduino-based low-cost meteorological measurement system: 2 m air and surface temperature, two levels soil moisture (volumetric water content) and temperature (5 and 20 cm); 2 m relative humidity, 2 m pressure, global radiation, 2 m wind speed and direction |
| Two Heitronics CT15.85 IR pyrometers | Ground temperature (north-pointing) and SST (south-pointing) |

***Ferryland supersite.*** Ferryland had two densely instrumented subsites called the Downs [a thin promontory protruding into the Atlantic, ~32 m above mean sea level (MSL)] and Battery (agricultural area, 3 m MSL), accompanied by two satellite sites, Beach House (21 m MSL) and Judges Hill (~129 m MSL). Figure ES1a shows an overview.

The Downs (Fig. 2a) had unabated exposure to easterly winds (E) and exposure to northerly (N) and southerly (S) winds with minor disturbances from isolated small islands. It was the most extensively instrumented, with some redundancies to ensure adequate data collection and instrument intercomparisons. The site had two Doppler lidars in a coordinated dual-Doppler scanning configuration with the partner lidars at Battery and Beach House; two Sonic Detection and Ranging Radio Acoustic Sounding System (Sodar-RASS) wind and temperature profiling systems; a fully instrumented flux tower with an energy balance station; a tripod with meteorological, flux, radiation, turbulence, and energy budget instrumentation; and the

**Table 3. Measurement instruments deployed during C-FOG for Battery site.**

| Instrument or instrument system/platform | Measured or retrieved parameters |
|---|---|
| Streamline$^{XR}$ lidar | Wind speed and direction |
| Radiometrics 3000 A microwave radiometer (MWR) | *T*, water vapor, liquid water, RH, and LWC profiles |
| Vaisala PWD52 visibility sensor | Visibility |
| Vaisala CL31 ceilometer | As above |
| Metek MRR-2 Micro Rain Radar | Doppler spectra of hydrometeors; derived precipitation rate (PR) and amount (PA) |
| Flux tower (15 m) on a grassy field: five levels of CSI CSAT-3 sonic anemometers, CSI model E-Type fine-wire thermocouples and Vaisala HMP-155 T/RH sensors (1, 2, 5, 8, 15 m); two levels of CS EC150 open-path $CO_2$/$H_2O$ gas analyzers (2 and 15 m); two levels of up- and downfacing K&Z CGR4 pyrgeometers (8 and 14 m); two Hukseflux HFP01SC ground heat flux plates buried at –10 cm; CS soil moisture sensors CS616, buried at –10.5 cm; CS soil thermocouples TCAV (E-Type) buried (–5 and –8 cm) | Three components of velocity, temperature, $CO_2$ and $H_2O$ fluxes, radiation, ground heat flux, and soil moisture |
| Four-component surface radiation balance, with pairs of K&Z CGR4 pyrgeometers and CMP21 pyranometers (2 m) on a sawhorse platform within a few meters of the tower base | IR and SW radiative fluxes; looking up and down; derived albedo, net radiation flux at 2 m |
| A pair of K&Z CGR4 pyranometer and pyrgeometers 2 m over the rocky shore | LW net radiation at the shoreline |
| Omega E–type thermocouple submerged in the ocean | Water temperature (low tide would not uncover it) |
| AlphaSense OPC-N2 | Aerosol monitor (number and mass concentration) |
| DMT FM100 Fog Monitor | Fog droplet spectra |
| Adolf Thies GmbH Laser Precipitation Monitor (LPM) | Rain droplet spectrum and fall velocity |

**Table 4. Measurement instruments deployed during C-FOG for Judges Hill (JH) and Beach House (BH) sites.**

| Instrument or instrument system/platform | Measured/retrieved parameters |
|---|---|
| LEMS at JH | Energy balance |
| Moutrie time-lapse camera at JH | Pictures of Battery site |
| PWD22 at JH | As above |
| Streamline$^{XR}$ lidar and synchronizing antennas at BH | As above |

**Table 5. Measurement instruments deployed during C-FOG for Blackhead site.**

| Instrument or instrument system/platform | Measured or retrieved parameters |
|---|---|
| Flux tower (10 m): three levels of CS CSAT3 sonics, Rotronics HC2-S3 *T*/RH sensors and CS FW1 E–type fine-wire thermocouples (2, 5, 10 m); CS EC150 open-path gas analyzer (10 m); two levels of K&Z CNR1 and CNR4 four-component radiometers (1 and 4 m). Also 2 HFP01SC heat flux plates buried at –8 cm, CS 655 soil moisture probe buried –4.5 cm; Soil thermocouples CS TCAV (E-Type) buried –1 and –6 cm, all 50 m from the tower | Energy budget |
| LEMS 100 m northwest of the flux tower | As above |
| LEMS at Petty Harbor–Maddox Cove (located 43 km SW of the Blackhead site) | As above |
| Vaisala CL31 ceilometer | As above |
| Metek MRR-2 Micro Rain Radar | As above |
| PWD50 visibility sensor | Visibility (Vis), PR, PA, and precipitation type |
| AlphaSense OPC-N2 | As above |
| Adolf Thies GmbH Laser Precipitation Monitor (LPM) | Amount, intensity, and droplet spectrum of rain |
| Vaisala DigiCORA tethersonde system suspended with tethersonde TSS111 and AlphaSense OPC-N2 | Vertical profiling of meteorological and aerosols |

**Table 6. Measurement instruments deployed during C-FOG for Flatrock site.**

| Instrument or instrument system/platform | Measured or retrieved parameters |
|---|---|
| LEMS-1 at the sea level | As above |
| LEMS-2 on the ridge | As above |
| Moutrie game camera (time lapse) | Pictures—view of ridgeline LEMS |
| PWD22 Visibility Sensor at 300 from the sea level LEMS-1 | As above |
| AlphaSense OPC-N2 next to PWD22 | As above |
| CL31ceilometer next to PWD22 | As above |

**Table 7. Measurement instruments deployed during C-FOG for Osborne Head Site (Canada DND Meteorological Facility).**

| Instrument or instrument system/platform | Measured or retrieved parameters |
|---|---|
| Vaisala CL31 ceilometer | As above |
| 10 m flux tower: three levels of RMY 81000 sonics (2, 5, and 10 m sonics), two levels of HC2-S3 *T*/RH probes (2, 10 m); LI-COR 7500 A (2 m) | As above |
| Standard meteorological data from DND (PWD, met sensors) | *T*, dewpoint, RH, wind speed and direction, Vis, PR, and PA |

**Table 8. Measurement instruments deployed during C-FOG for R/V *Hugh R. Sharp*.**

| Instrument or instrument system/platform | Measured or retrieved parameters |
|---|---|
| Bow mast: three levels of HMP155 T/RH probes (7, 9, and 12.5 m); CSI IRGASON at12.5 m; K&Z CNR4 net radiometer at 11.5 m; VectorNav VN100 IMU and Trimble BX982 Dual-GNSS receiver for motion correction | As above |
| AlphaSense OPC-N2 | As above |
| TSI MOUDI Impactor for sampling particulate matter in terms of mass and chemical content | Morphology and chemical composition of size-segregated aerosols |
| Motion-stabilized Halo Photonics Streamline$^{XR}$ lidar | As above |
| Vaisala CL31 ceilometer | As above |
| Metek MRR-2 Micro Rain Radar | As above |
| Radiometrics 3000 A MWR | As above |
| PWD22 visibility sensor | As above |
| FM120 cloud-particle spectrometer | Fog droplet spectra is used for $N_c$, $r_e$, LWC, and Vis |
| Gondola platform: Combination of two droplet spectrometers, DMT CDP-2; DMT backscatter cloud probe BCP | CDP-2 for droplet spectra and BCP for droplet spectra derived: $N_c$, $r_e$, LWC, and Vis |
| Tethered lifting system (TLS), CIRES/NOAA/ARL, custom made | ABL meteorological profiling, custom turbulence package with fine cold-wire (CW) and hotwire (HW) for turbulence and mean of *T* and winds. $C_T^2$ and energy dissipations rate are calculated. |
| Vaisala RS41-SGP radiosonde launches and DigiCORA Sounding System MW41 | As above |
| Sky camera | Video of weather conditions |
| Rockland Scientific Vertical Microstructure Profiler (VMP) with shear probes, high-resolution thermistors and micro-conductivity/temperature (CT) sensors. | Depth variation of ocean turbulent kinetic energy dissipation rate and salinity–temperature–depth to a depth of 250 m |
| RMRCo Remote Ocean Sensing Radiometer (ROSR) | Sea surface skin temperature (SSST) |
| Seasnake system | (Bulk) SST at 1–3 cm depth via a chain of floating thermocouples |
| DU Instrument Cluster: custom-built fog inlet that segregates droplets and particles larger and smaller than 2.5 $\mu$m; TSI-DMA model 3081 CPC 3772 Scanning Mobility Particle Sizer (SMPS); TSI-3032 Aerodynamic Particle Sizer (APS); DMT CCN-100 Cloud Condensation Nuclei Counter (CCNC); Aerodyne Aerosol Chemical Speciation Monitor (ACSM) | Dried aerosol spectra from 10 to 450 nm (SMPS) and 0.5 to 20 $\mu$m (APS); CCN concentrations at selected supersaturations (CCNC); non-refractory aerosol chemical composition, reports sulfate, nitrate, ammonium, and organics (ACSM) |

NPS Aerosol Sampling Unit (NASU) trailer with a suite of microphysical instruments. Also at Downs were a ceilometer, two types of Scintillometer transmitters, a custom-built Local Energy Budget Measurement Station (LEMS), a radiosounding station, and a micrometeorological balloon-based tethered observing system (DUMBO).

Battery's (Fig. 2a) instrumentation consisted of a lidar, microwave radiometer (MWR), visibility sensor, ceilometer, Micro Rain Radar (MRR), flux tower, four-component surface radiation balance, SST sensor, and microphysical instrumentation consisting of an aerosol monitor, a fog monitor, and Laser Precipitation Monitor (LPM).

Judges Hill satellite site had a LEMS, time-lapse camera, and a present weather detector (PWD) for visibility (see Fig. ES1b). Beach House housed a lidar and synchronizing antennas.

***Blackhead site.*** This site (Fig. 2b) included a fully instrumented flux tower with an energy balance station, a ceilometer, MRR, PWD, and micrometeorological sensors. Vertical fog microstructure profiling was conducted using a tethersonde system suspended with meteorological and aerosol instrumentation. Petty Harbor–Maddox Cove was a satellite site near Blackhead with an LEMS (Fig. ES1b).

***Flatrock site.*** Instrumentation here was distributed over three proximate locations (Fig. 2b): a LEMS near the sea level, an LEMS and time-lapse camera on the ridge of the peninsula, a visibility sensor, ceilometer, and aerosol samplers.

***Osborn Head site.*** This site at the DND meteorological facility in NS (Fig. 2c) included a ceilometer and a flux tower. Standard data collected by DND, such as visibility, wind speed and direction, temperature, pressure, and radiation, were available for C-FOG research.

***R/V* Hugh R. Sharp.** The instrumentation on R/V *Sharp* included (Fig. 2d) a fully instrumented bow mast (flux tower), ceilometer, micro-orifice uniform deposit impactor (MOUDI), fog water collector, motion-stabilized lidar, MRR, MWR, visibility sensor, cloud-particle spectrometer, a gondola-shaped platform carrying droplet spectrometers, a tethered lifting system (TLS) for meteorological profiling, a radiosounding system, sky camera, vertical microstructure profiler (VMP) for the depth variation of ocean turbulent kinetic energy dissipation rate and salinity/temperature, a remote ocean sensing radiometer (ROSR) for (skin) SST, and a Seasnake system for (bulk) SST. The Dalhousie University (DU) instrument cluster operated behind a custom-built fog inlet that segregated droplets and included an array of aerosol number counting, sizing, and chemical characterizing instruments (Tables 2–8).

While most of the equipment acquired data continuously, special instruments such as TLS were operational only during the intensive operational periods (IOPs), whence all measurement systems were a go. During the campaign, daily radiosondes were released from the sites and the R/V *Sharp* at 0000 and 1200 UTC, except during IOPs when they were released every 3 h.

## Data repository

Campaign data, notes, and photographs from the C-FOG campaigns are stored at repositories from individual groups (see sidebar) as well as in a Google Team Drive at the University of Notre Dame (UND). After full quality control/quality assurance, the data will be publicly available in June 2021.

## IOP periods

Daily weather briefings were conducted at 13.00 Newfoundland daylight time (UTC – 2.5 h; EST + 1.5 h), wherein the forecasts of climatological (Scripps), satellite (ECCC, UOIT), and

modeling (NRL, ECCC) products were synthesized. The "present conditions" using climatological methodology were obtained from an assortment of infrared and visible satellite images, three Atlantic Canadian sounding stations (Fig. 1), four radar stations, and selected surface stations reporting visibility, clouds, and weather (one being St. John's International Airport). The Scripps forecast also consulted CMC-HRDPS, GFS, and RAP[1] modeling systems. The ECCC predictions for 1200 and 1800 UTC utilized several operational NWP models (WRF, GFS, HRDPS, NAM, and Rapid RUC). Data fusion of numerical forecasts, together with *GOES-16* fog products and ECCC C-band radar images, were also used for prediction of fog conditions by melding EEEC forecast products using artificial intelligence, which provided probabilistic forecasts of no (0%), light (50%), or heavy (100%) fog.

In parallel, COAMPS[2] runs by NRL-provided forecasts four times a day (0000, 0600, 1200, and 1800 UTC). Predicted fields with lead times of 18–36 h were used, occasionally extending out to 48 h. COAMPS lateral boundary conditions were provided by NAVGEM (32 km average grid spacing), while the 3DVar data assimilation method helped prepare initial conditions. There were three telescopically nested grids of spacing of 18, 6, and 2 km. The fourth fine grid at 2 km initially covered R/V *Sharp*, but was eventually switched off due to time lag in receiving planned ship track. There were 60 vertically stretched model levels with the model top just below 30 km. Nearest to the surface were 15 levels in the lower 1 km of the atmosphere (see "Numerical modeling overview" section in the supplemental material for details).

[1] For AMS standard abbreviations, see www.ametsoc.org/ams/index.cfm/publications/authors/journal-and-bams-authors/formatting-and-manuscript-components/list-of-acronyms-and-abbreviations/.

[2] COAMPS is a registered trademark of the U.S. Naval Research Laboratory.

A go–no-go call for an IOP as well as its start and stop time were made a day ahead once consensus was reached on the likelihood of fog occurrence based on all input data and assessment by project personnel. Twelve IOPs were called (Table 9), typically 1 day long, except the Super IOP10 that lasted 3 days. Only 6 out of 12 IOP fog calls were an observational success. The ship assets were mostly run continuously except the radiosondes and TLS, and potential fog periods or ship IOP (SIOP) alerts were relayed to the R/V *Sharp* during daily meetings; three of the six fog alerts became reality (Table 10).

Hindcasting of IOPs was made using the WRF Model (V3.9; Skamarock et al. 2008). Five nested domains were used, with the innermost domains covering NS and NL where the field sites were located (see "Numerical modeling overview" section in the supplemental material). One of the domains covered the R/V *Sharp*'s path. In high-resolution WRF runs, 1 km horizontal resolution and 50 or 100 irregularly stretched vertical levels, with greater grid density inside the ABL, were used. Both COAMPS and WRF were employed to evaluate NWP model efficacy as a forecasting tool, to guide interpretation of flow and fog patterns, and to elicit underlying physical processes.

## Results

For brevity, selected representative results from IOP/SIOPs and simulations are described below, leaving full technical results to be described in future archival papers, including a special issue of *Boundary-Layer Meteorology*.

***Ship observations.*** SIOP1 is a vivid example of how integrative, multiplatform, multiscale analyses could be used to analyze fog events. While off the coast of NL on 13 September, the R/V *Sharp* encountered two periods of fog (0000–0300 and 0500–0700 UTC) as evident from ceilometer and visibility data (Figs. 3a,b,e), but no fog was present at the land sites. On the R/V *Sharp*, true winds were southerly (RH ~ 95%) with patchy stratus aloft until 2200 UTC 12 September [Figs. 3b,e; Fig. 4b(i)]. The winds gradually changed to northerly (RH ~ 100%) at 0000 UTC 13 September. The R/V *Sharp*'s 12.5 m air temperature ($T_a$) fell

below the SST with $\Delta_{a-s} = T_a - \mathrm{SST} = -0.5°\mathrm{C}$ (Fig. 3e), which marked the appearance of fog, yet without signs of stratus lowering (Fig. 3b). The rapid shift of wind direction signifies a

**Table 9. IOP fog forecasts and occurrences.**

| | IOP start/end | Ferryland | Blackhead/Flatrock | Notes |
|---|---|---|---|---|
| IOP1 | Start: 1430 UTC 5 Sep<br>End: 1430 UTC 6 Sep | No fog | No fog | Fog was observed on 4 September over the Ocean and Flatrock sites, but not during the IOP |
| IOP2 | Start: 1430 UTC 7 Sep<br>End: 2030 UTC 7 Sep | No fog | No fog | |
| IOP3 | Start: 0930 UTC 8 Sep<br>End: 1230 UTC 8 Sep | Fog | No fog | Fog was observed for very short duration from the southwest of Ferryland |
| IOP4 | Start: 0220 UTC 10 Sep<br>End: 0800 UTC 11 Sep | No fog | Light fog at Blackhead | |
| IOP5 | Start: 2030 UTC 11 Sep<br>End: 1130 UTC 12 Sep | No fog, light stratus | No fog | |
| IOP6 | Start: 1830 UTC 13 Sep<br>End: 1130 UTC 14 Sep | Patches of reduced visibility | Fog at both | ShiPnear the Blackhead |
| IOP7 | Start: 0000 UTC 16 Sep<br>End: 1430 UTC 17 Sep | Light patchy fog at 1200 and 1600–1700 UTC | Fog, dissipated quickly | Fog at St. John's |
| IOP8 | Start: 1730 UTC 21 Sep<br>End: 0230 UTC 22 Sep | No fog | No fog | Very low temperatures (8–9°C at Ferryland) |
| IOP9 | Start: 0230 UTC 23 Sep<br>End: 1430 UTC 24 Sep | Mist, low visibility until 1400 UTC | Similar conditions offshore | Power outage |
| IOP10 | SUPER-IOP<br>Start: 1730 UTC 27 Sep<br>End: 0330 UTC 30 Sep | 27 Sep: Misty with decreasing visibility as the day progressed | 27 Sep: No fog, short period of rain, post sunrise low stratus | Low visibility over ocean most of the time |
| | | 28 Sep: Patchy fog | 28 Sep: Early morning rain, afternoon drizzle and mist, stratus lowering throughout day, short (1 h) period of evening fog with wind shift to north; patchy fog at night | |
| | | 29 Sep: Patchy fog | 29 Sep: low stratus, mist, drizzle before noon, sporadic and patchy fog due to stratus lowering | |
| | | 30 Sep: Patchy fog | 30 Sep: Morning drizzle changing to rain, patchy stratus, shift to northerly flow | |
| IOP11 | Start: 2030 UTC 30 Sep<br>End: 0230 UTC 1 Oct | No fog | No fog | Low visibility over water. Fog at St. John's NL airport. |
| IOP12 | Start: 2030 UTC 3 Oct<br>End: 1430 UTC 4 Oct | No fog, but over ocean | No fog | Fog in Halifax |

**Table 10. Ship fog occurrences.**

| Ship observations of fog days | Ship IOP start/end | Location | Notes |
|---|---|---|---|
| SIOP1 | Start: 1700 UTC 12 Sep<br>End: 0700 UTC 13 Sep | Northeast of St. John's, Newfoundland | No visible stratus before fog appearance |
| SIOP2 | Start: 0900 UTC 28 Sep<br>End: 1600 UTC 28 Sep | West-southwest of Nova Scotia | Stratus lowering |
| SIOP3 | Start: 20:00 UTC 4 Oct<br>End: 22:30 UTC 4 Oct | East of Cape Cod, Massachusetts | Stratus lowering |

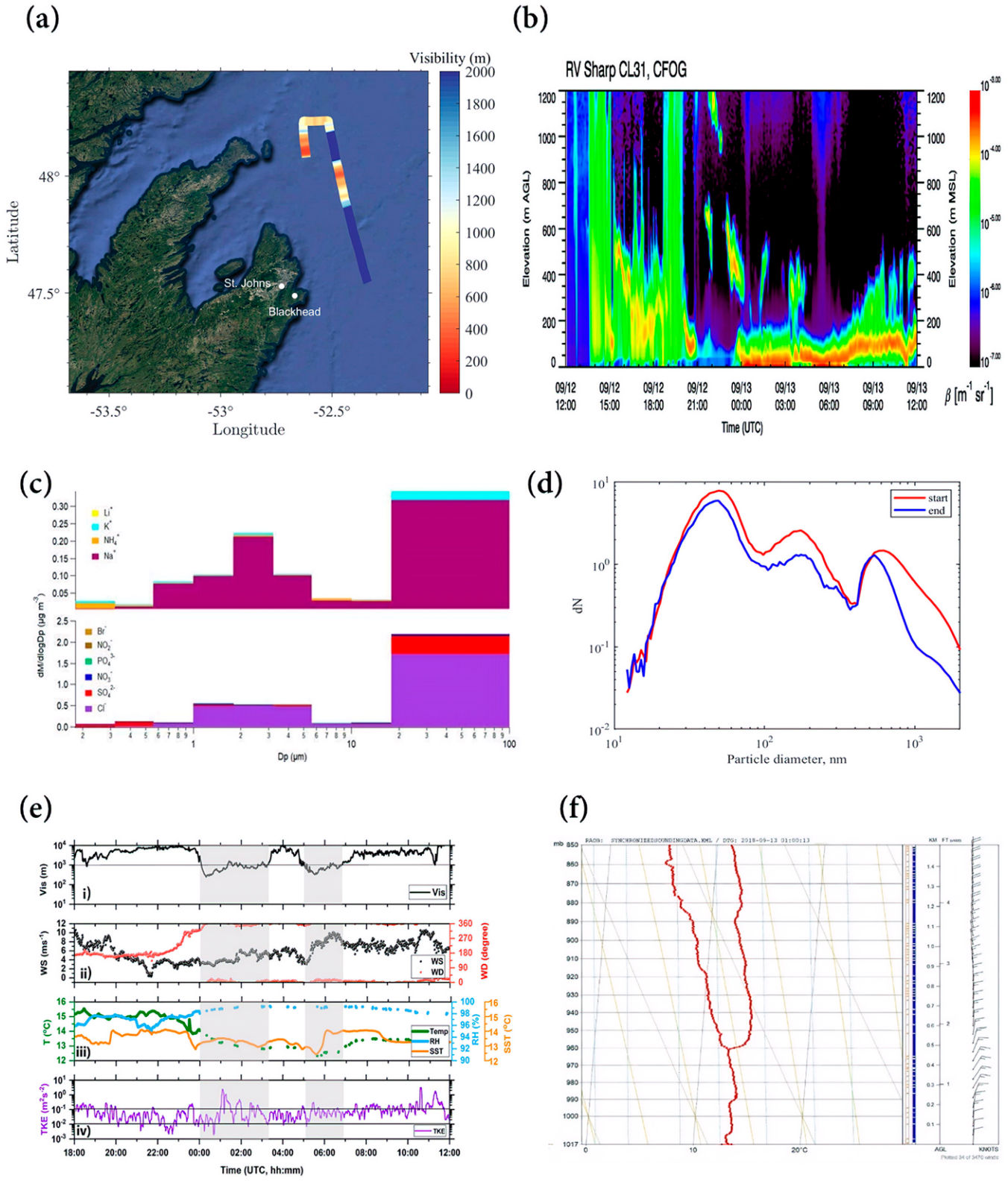


**Fig. 3. (a) The ship track during SIOP1, with the visibility in the color bar. (b) Ceilometer backscatter with time, indicating the height of the fog layer/cloud base. (c) (top) Cation and (bottom) anion analysis as a function of aerodynamic diameter $D_p$ from MOUDI Impactor, from Stack A installed 0104 UTC 13 Sep and removed 1036 UTC 14 Sep (analysis by Dr. Trevor VandenBoer, York University). (d) Average particle number size distribution dN during the first (red) and last (blue) 30 min of SIOP1 as measured through the droplet line of the DU instrument cluster. Data have not been corrected for transmission efficiency of the inlet. This shows the aerosol particle number size distributions from 0000 to 0003 UTC for event during SIOP1. Between red and blue lines, the particle number concentration reduced by 33%. During the same period of the second event (0500–0700 UTC), the reduction was 80% (not shown). (e) A time series of (top to bottom) visibility; wind speed and direction; air temperature *T*, SST, and RH; and turbulent kinetic energy (TKE) during SIOP1, starting at 1800 UTC 12 Sep. (f) Tephigram plot from the radiosonde released at 0100 UTC.**

northeastward-traveling synoptic pressure system, which is typical of the Canadian Atlantic summer (Dorman et al. 2020; Dorman et al. 2021). Before the shift, R/V *Sharp* was on the edge of an anticyclone [southerly winds and patchy clouds; Figs. 4a,b(i)], followed by the influence of a northerly branch of a cyclone [Figs. 4a,b(ii)], signifying local mesoscale response to a traveling synoptic system. Saturated conditions, lower $T$, moderate turbulence (TKE ~ 0.1 $m^2$ $s^{-2}$; Fig. 3e) all contributed to near-surface fog formation at 0000 UTC. Taken together, these observations suggest that SIOP1 is a case of *advection cold fog*.

Interestingly, the northerly flow is saturated up to ~500 m (Fig. 3f), while the fog layer near the surface indicated by ceilometer extends to ~50 m [Fig. 3b, no clouds in Fig. 4b(ii)]. Possibly the dense fog layer contributed by higher near-surface $N_c$ impedes ceilometer backscatter from possible fog at higher levels, particularly from beyond ~200 m. This notion is supported by deeper penetration of ceilometer signal during ephemeral drop of surface fog density. The MOUDI-based chemical analysis shows hygroscopic sea salt (NaCl) particles with a bimodal distribution ($D_p$ ~ 1–100 $\mu$m) (Fig. 3c) as the dominant aerosol constituent (>1 $\mu$m). As for FCN, hygroscopic ammonium sulfate would have been the most effective as its $N_c$ would have been far higher due to smaller sizes (<0.3 $\mu$m). According to Pósfai et al. (1999), the entire submicron fraction of North Atlantic marine boundary layer aerosols is dominated by ammonium sulfate, and some of which are too small to be resolved by MOUDI. The desiccated samples of CNs during the fog were in the range 10 nm–1 $\mu$m, and during SIOP1 their number concentration gradually decreased, possibly by mixing with overlying air, scavenging, or wet deposition (Fig. 3d). Other microphysical characteristics, including LWC, $N_c$, and MVD obtained from the gondola-based (CDP and BCP), and FM120 measurements are shown in Fig. 5. Differences seen are likely due to their relative locations on the ship and resolvable size ranges.

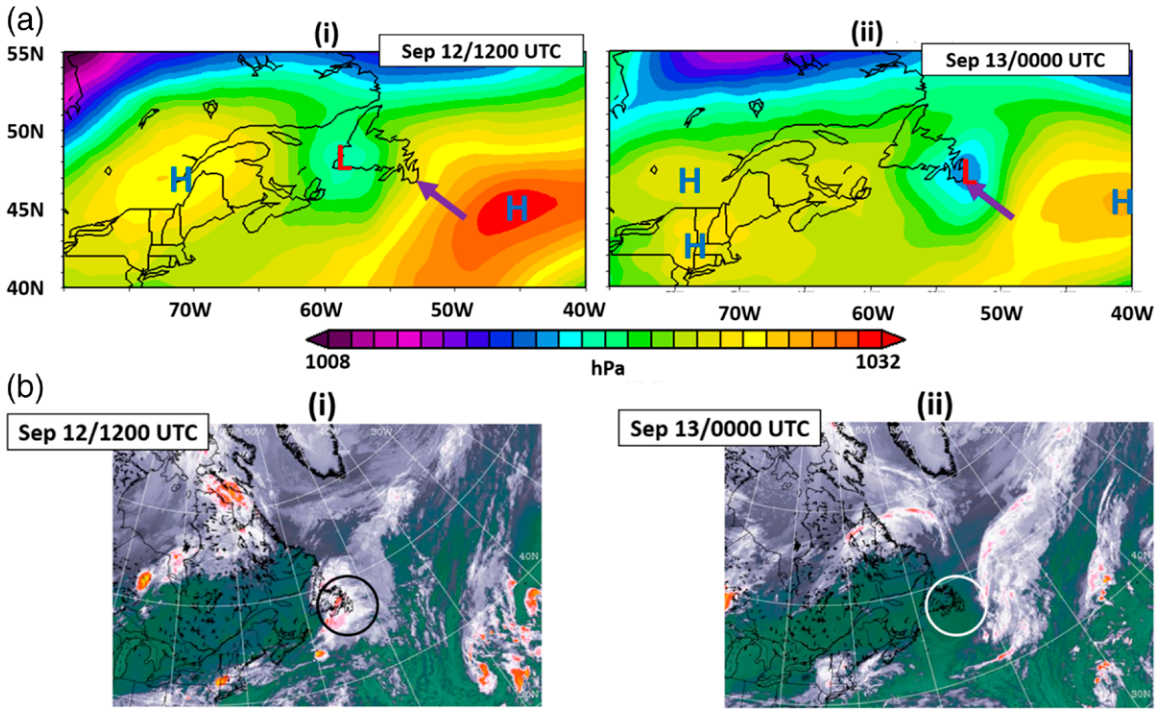


**Fig. 4. (a) NARR SLP analyses for 1800 UTC 12 Sep to 0000 UTC 13 Sep (NARR provided by the NOAA/OAR/ESRL/PSD at www.esrl.noaa.gov/psd/). The arrow points to Avalon Peninsula. (b) GOES-East IR images for the same period, showing the absence of significant stratus lowering during fog formation at 0000 UTC. Circles are centered over the Ferryland. The ship was to the northeast and within the circles. Fog was observed in Ferryland at 1200 UTC 12 Sep but by the time of SIOP1, Ferryland was devoid of fog.**

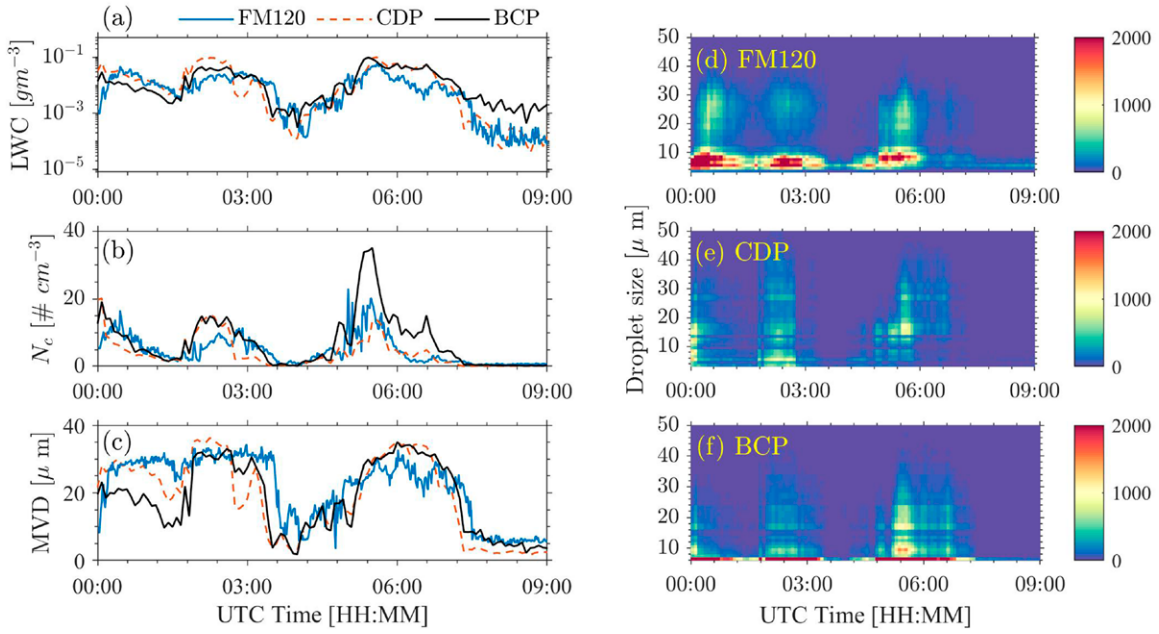


**Fig. 5. (a)–(c) LWC, $N_c$, and MVD time series (13 Sep). Blue, dashed red, and black lines represent FM120 (range: 1–50 $\mu$m), CDP (2–50 $\mu$m), and BCP (5–100 $\mu$m) measurements, respectively. Droplet bin midsize ($y$ axis) time series with raw droplet counts (color bars) for (d) FM120, (e) CDP, and (f) BCP probes. The CDP and BCP were mounted on the gondola platform located ~10 m above the lower deck level.**

The persistence and dissipation of fog during SIOP1 provide insights into the fog life cycle. The synoptic forcing was nominally stable and $\Delta_{a-s} = T_a$ – SST during the entire SIOP1, and fog responded in kind until ~0300 UTC, whence it dissipated quickly. An increase of wind speed from 4 to 6 m $s^{-1}$ during the first fog event led to an order of magnitude increase of TKE, which might have been responsible for the breakup of inversion that tops the fog layer and enhanced vertical mixing (Figs. 3b,e). Arguably, the subsequent decay of turbulence and reduction of wind speed might have restored the fog layer at 0500 UTC, but thereafter the wind speed (4–10 m $s^{-1}$) and TKE increased again, aided by convective forcing due to increase of $\Delta_{a-s}$, thus promoting entrainment at the fog top, increasing the surface mixing-layer depth, slightly reducing the surface RH and leading to dense lifted fog at an altitude of >50 m after 0700 UTC. A radiosonde launched at 0813 UTC shows that near-saturated air still persisted up to ~700 m (not shown), and thus it is possible that fog was present beyond this dense fog layer but its backscatter signal was obscured by denser fog below.

***Observations at Ferryland.*** The Downs recorded typical eastward-/northeastward-propagating synoptic weather systems with pressure oscillations in the range ~1,000–1,030 hPa (Fig. 6a). A general observation was that low pressure conditions showed a propensity for fog, but rain and strong winds exceeding 10 m $s^{-1}$ often suppressed fog formation. Fast response sonics recorded gusts reaching 20 m $s^{-1}$. Wind flow was predominantly southwesterly/westerly (SW/W) and northerly/northeasterly (N/NE), with mean temperature in N/NE winds ~3°C cooler than SW/W winds. A drop in temperature below ~10°–12°C during N/NE wind episodes was conducive for fog formation. Moreover, the temperature distributions were positively and negatively skewed for SW/W and N/NE flows, respectively. The data did not show significant specific humidity differences linked to the wind direction change (not shown). Successful IOPs with fog (green shading) are associated with near saturation of air (Fig. 6a). Signatures of fog were also evident as perturbations to the diurnal variability of radiation flux and soil

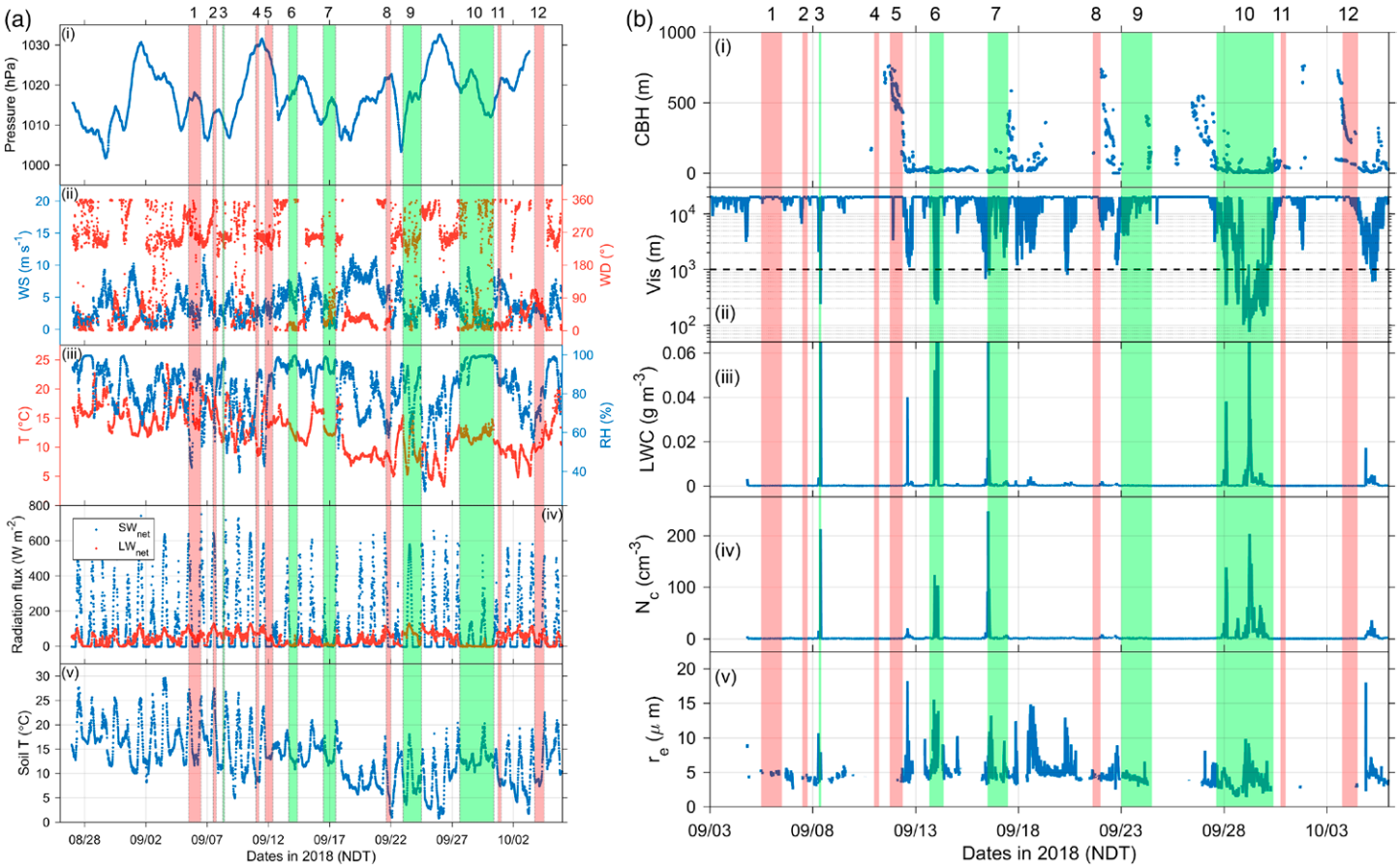


**Fig. 6. (a) (i) Pressure, (ii) wind speed and direction, (iii) temperature and RH, (iv) net shortwave and longwave radiation flux, and (v) soil temperature at Downs. Columns with green shading show IOPs with fog (or mist) and light red shading shows IOPs with no fog at Downs. The IOP number is indicated at the top. (b) Ceilometer, PWD, and CDP observations at Downs. (i) Cloud-base height (ceilometer), (ii) visibility (PWD), CDP estimates of (iii) liquid water content, (iv) droplet number concentration ($N_c$), and (v) the effective radius $r_e$ (area-weighted mean radius of the droplets that signifies their effect on radiation). Droplets in mist (~1 $\mu$m) period (IOP9) are not well captured by CDP (2–50 $\mu$m).**

temperature, most prominently during the IOP7 and IOP10 (Fig. 6a). Fog development did not occur during IOP9, but misty conditions prevailed at Downs.

The low cloud base height (CBH) measured by the ceilometer during IOPs 6, 7, and 10 indicated fog, consistent with visibility and microphysical data (Fig. 6b). Comparison of fog microphysical data from NL coastal fog with U.S. West Coast fog observations at Marina, California (Daniels 2019), indicates that LWC and effective radius ($r_e$) were higher at Marina (not shown), although $N_c$ was comparable. The differences could be attributed to the origin of fog. At Marina, fog that forms over the ocean is advected toward land whereas at Downs the terrain-induced flow and terrestrial aerosols affect fog formation. This emphasizes the need for accurately accounting for both local and background environmental conditions in fog forecasting models.

***Transient mixing fog at Downs.*** An interesting case of fog that lasted only tens of minutes occurred on 16 September during IOP7. Starting at ~0000 UTC, the winds were westerly at ~8 m s$^{-1}$, and then started to subside (~2 m s$^{-1}$) at ~1030 UTC and changed direction to northwesterly (not shown). This was followed by a curious event at ~1145 UTC, where the wind speed momentarily increased to ~6 m s$^{-1}$, TKE and TKE dissipation rate ($\varepsilon$) increased fourfold to sixfold, $T$ decreased, and RH approached saturation (Fig. 7). Minutes thereafter, TKE and $\varepsilon$ decayed, winds were stagnant, RMS temperature fluctuations $\sigma_\theta$ increased significantly, suggesting the arrival of the front of a northeasterly colder, saturated air mass, its

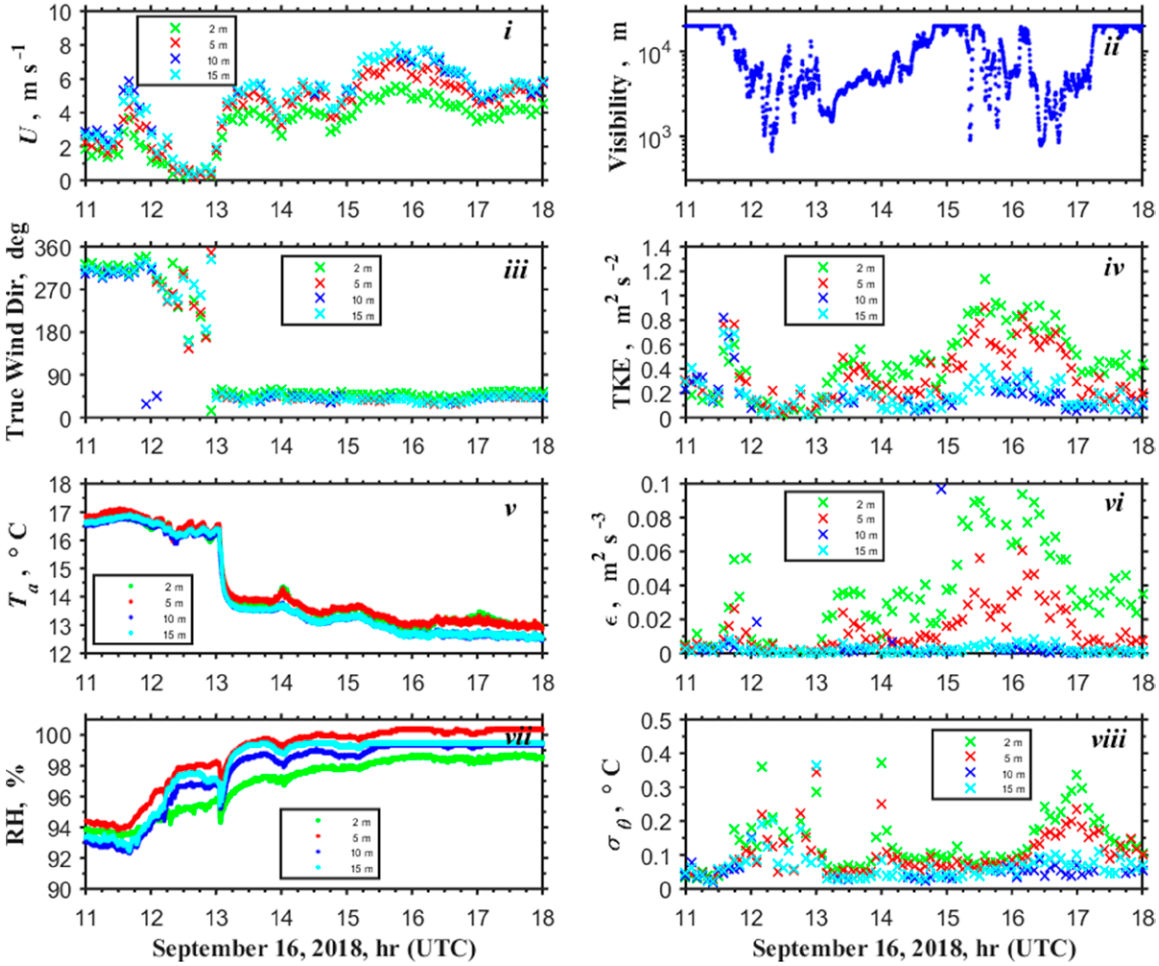


**Fig. 7. Time series of (i) wind speed, (ii) visibility, (iii) wind direction, (iv) TKE, (v) air temperature, (vi) TKE dissipation rate, (vii) relative humidity, and (viii) standard deviation of sonic temperature at four levels based on the data collected at Downs 16.2 m flux tower during IOP7. Temperature (*T*) and relative humidity (RH) measurements were made by the slow-response (1 Hz) *T*/RH sensors and 1-min-averaged visibility was measured by PWD22. Wind speed and direction and turbulent statistics are based on 5-min-averaged sonic anemometer measurements. Data processing techniques are the same as in Grachev et al. (2018).**

impingement on Downs topography, and mixing between this colder air mass and surrounding near-saturated warmer air masses. Simultaneously, localized fog appeared enveloping the Downs at ~1215 UTC and lasting for about 15–20 min. This is clearly evident from the visibility (Fig. 7) as well as dual Doppler lidar and camera (Fig. 8) observations. During the ensuing mixing and stagnation event, visibility fluctuated (Fig. 7) and patchy fog appeared, followed by continuation of the northeasterly flow for another 3 h wherein another fog event occurred at ~1630 UTC (not discussed here). Lidar backscatter (Fig. 8) shows that the thickness of the colder air mass as $h$ ~250 m (subcloud layer), and its observed speed ~6 m s$^{-1}$ is consistent with a gravity current propagation speed $\sqrt{g\Delta T h/T_0}$ ~5.9 m s$^{-1}$ (Simpson 1999), where $\Delta T$ (~4°C) is the temperature difference between the colder air mass and ambient air, $T_0$ is the reference temperature, and $g$ is the gravity. Overall, IOP7 can be interpreted as a mixing fog event induced by coastal topography. The air masses involved were in near saturation so that mixing between them, aided by resuspension of FCN over the landmass, may have provided conditions for fog genesis.

***Super IOP10 and EM propagation.*** Super IOP10 (27–30 September) provided comprehensive multiday information on microphysical, EM, and environmental variables. For example,

the data taken at Battery and Downs are shown in Fig. 9. Visibility and precipitation from the PWD at Battery on 28 September indicated several periods of low visibility (Fig. 9a). There was ~5 mm $h^{-1}$ precipitation in the morning until 0300 UTC, followed by fog, which dissolved again when rain started at 0400 UTC. Fog appeared at 0600 UTC after the rain ceased, lasting for half an hour (precipitation fog). A longer period (1200–1900 UTC) of drizzle ensued associated with precipitation, with fog appearing when the rain stopped intermittently. A lengthy fog period persisted (1900–2100 UTC) after precipitation stopped at 1900 UTC. The PWD visibility observations were consistent with ceilometer (Fig. 9b) and FMD100 (not shown) observations. The observations of rain obliterating fog as well as reemergence of fog after rain were consistent with those at the Downs. The observations at Judges Hill (~129 m MSL) were different, demonstrating the elevation (i.e., terrain) dependence of fog; here the fog events were abundant because of the hill's frequent shrouding by low-level stratus.

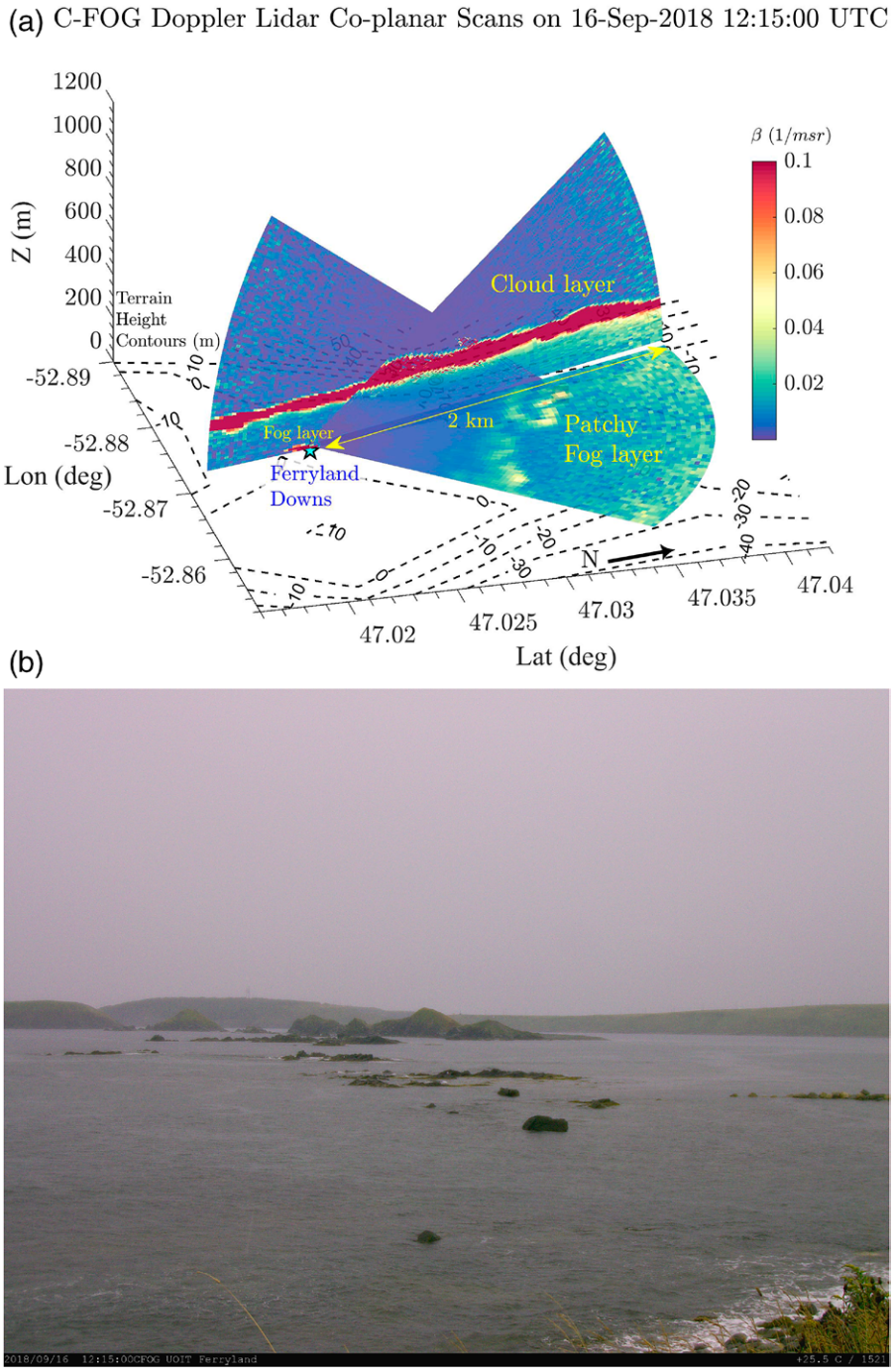


**Fig. 8. (a) Co-planar dual-Doppler lidar scans of range-corrected attenuated backscatter ($m^{-1}$ $sr^{-1}$) operating from Downs and Battery sites. Contours represent the terrain heights (m). High backscatter estimates represent clouds, fog, or a density inversion. The estimated fog layer thickness is ~45 m at the Downs. The elevated cloud layer is ~280 m MSL. The scans are mostly over water and the Downs. (b) A video frame from the Battery site taken at 1215:12 UTC, looking at Downs.**

Satellite and Battery sites at Ferryland were in continuous communication with Downs via EM remote sensors. In one study on EM transmission, an IR-MW band BLS900 scintillometer (Fig. 9c) with a transmitter (Battery) and receiver (Downs) pair located ~1.4 km apart was used. Optical particle counters at Battery provided a near-complete picture of the particle size spectrum ranging from 0.3 $\mu$m to 8 mm. While local PWDs showed some heterogeneity of visibility, with Downs reporting more fog periods, the good correlation between signal attenuation and the visibility from two PWDs located at each terminus suggests prospects of using

scintillometry as a future fog observation tool (Fig. 9c). Note that there are periods where Battery reported fog, but the scintillometer signal and the Downs PWD implied clear conditions (1700 UTC 28 September) and times when there was patchy fog at both the Downs and Battery but the scintillometer signal remained high (0300 UTC 28 September). The infrared signal decayed faster during heavy fog, and when the signal returned, it highlighted spatial variability within fog. Around 0400 UTC 29 September, the visibility increased to just below 1 km, and at this point, the scintillometer regained a readable signal before visibility reduced again. The signal only began spiking to readable levels after 1800 UTC 29 September, even though the Battery PWD was no longer consistently reporting fog from 1100 UTC 29 September. In all, a scintillometer could prove to be a useful tool for determining spatial characteristics of fog, as alluded to by Vasseur and Gibbins (1996).

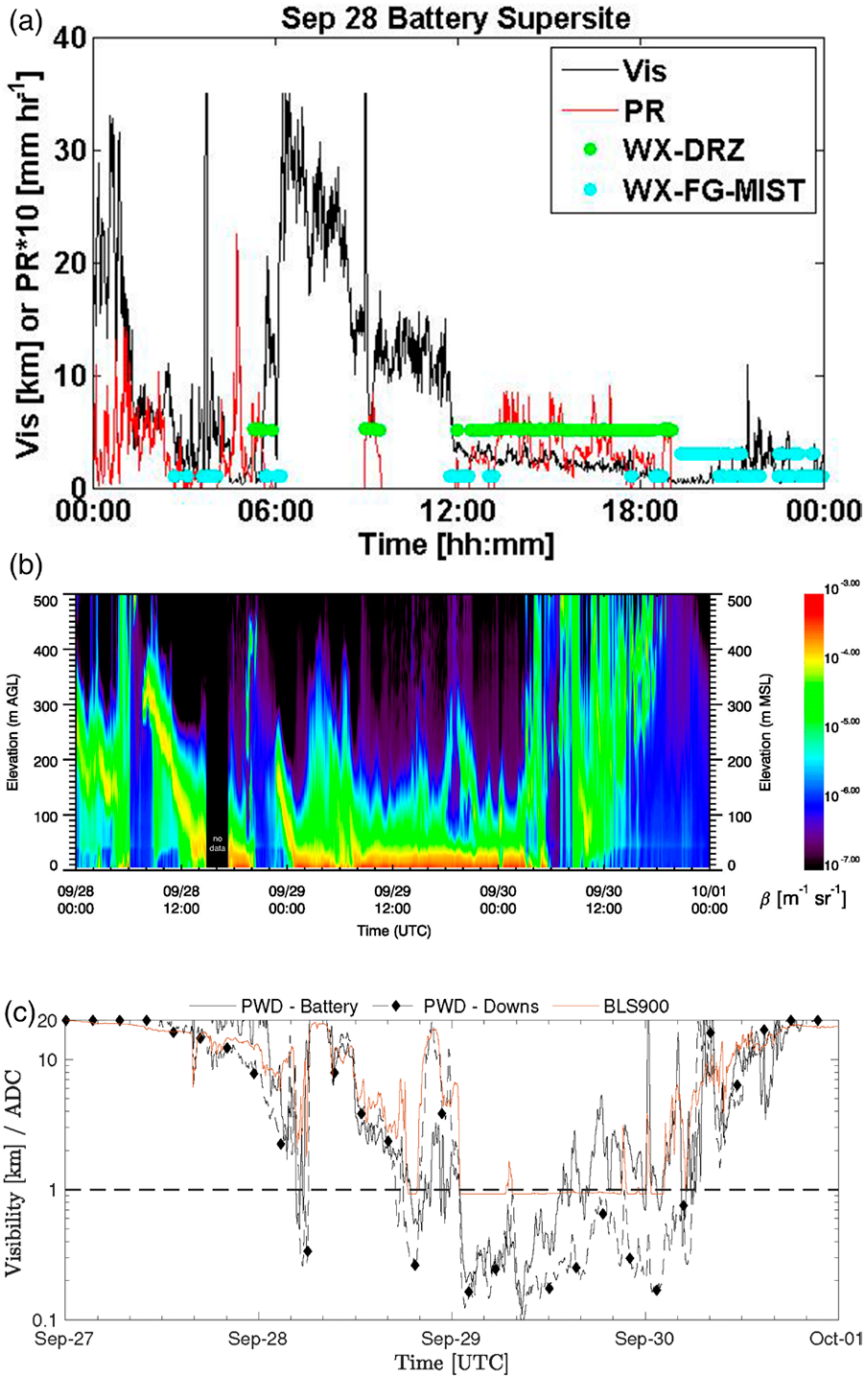


**Fig. 9. Data from Super IOP10. (a) Visibility (Vis), precipitation (PR), hydrometeor type (based on National Weather Service synoptic code) at the Battery site: WX-DRZ, drizzle; WX-FG-MIST, combination of fog and mist conditions. (b) CL31 ceilometer backscatter time–height cross section for Downs. (c) Time series of PWD visibility at Battery and Downs sites and scintillometer ADC (analog to digital converted output) scaled to fit the visibility axis.**

***Stratus lowering at Blackhead: Observations and WRF simulations.*** During IOP6 (13–14 September), the Blackhead site recorded an explicative 3 h coastal fog event. Unlike SIOP1 that occurred off the coast of Blackhead on the preceding day, this was a clear stratus lowering event, which followed light precipitation that produced high RH (~90%). Tethered balloon observations prior to the event indicated mixing between saturated and unsaturated air layers between the stratus (~150 m AGL) and beneath, with the inversion between the cloud and subcloud layers having $Ri_g \leq 0.25$ (calculated using 2 m resolution profiling data), characterizing sustained turbulence. The

air above the stratus deck was unsaturated (~40%), with no clouds evident from satellite imagery, and thus significant radiative cooling is expected at the cloud top. After sunset (2130 UTC 13 September), radiative cooling led to cloud-top instability and top-down turbulent mixing, causing enhanced TKE (~0.6 $m^2 s^{-2}$; Fig. 10a), downward mixing of moisture, evaporative cooling of falling droplets (MRR observations), slow descent (~0.1 $m s^{-1}$) or lowering of the cloud top to the surface (ceilometer), decrease of visibility, and increase of RH to 100% (Figs. 10a–c). Once the cloud lowered to the surface, TKE diminished to a sustained level of ~0.1 $m^2 s^{-2}$. The fog layer was extremely stable with $Ri_b$ ~10, and lasted for ~3 h. The wind direction remained northerly as before the event, and the cooling rate near the surface was weak and constant (~0.03 K $h^{-1}$). The dissipation of fog occurred due to intrusion of drier air from aloft and enhanced vertical mixing (TKE ~ 0.8 $m^2 s^{-2}$, $Ri_g \leq 0.25$; Fig. 10b), thus completing the life cycle.

The application of WRF-ARW to simulate IOP6 exemplifies its utility to guide interpretation of observations and NWP model validations (see "Numerical modeling overview" section in the supplemental material for details). WRF simulations were conducted for all IOPs with different default PBL and microphysical schemes. For IOP6, four microphysical and two PBL schemes were employed, guided by Lin et al. (2017). Only the NSSL 2-moment microphysical scheme (Mansell et al. 2010) was able to capture the fog life cycle with acceptable accuracy. The

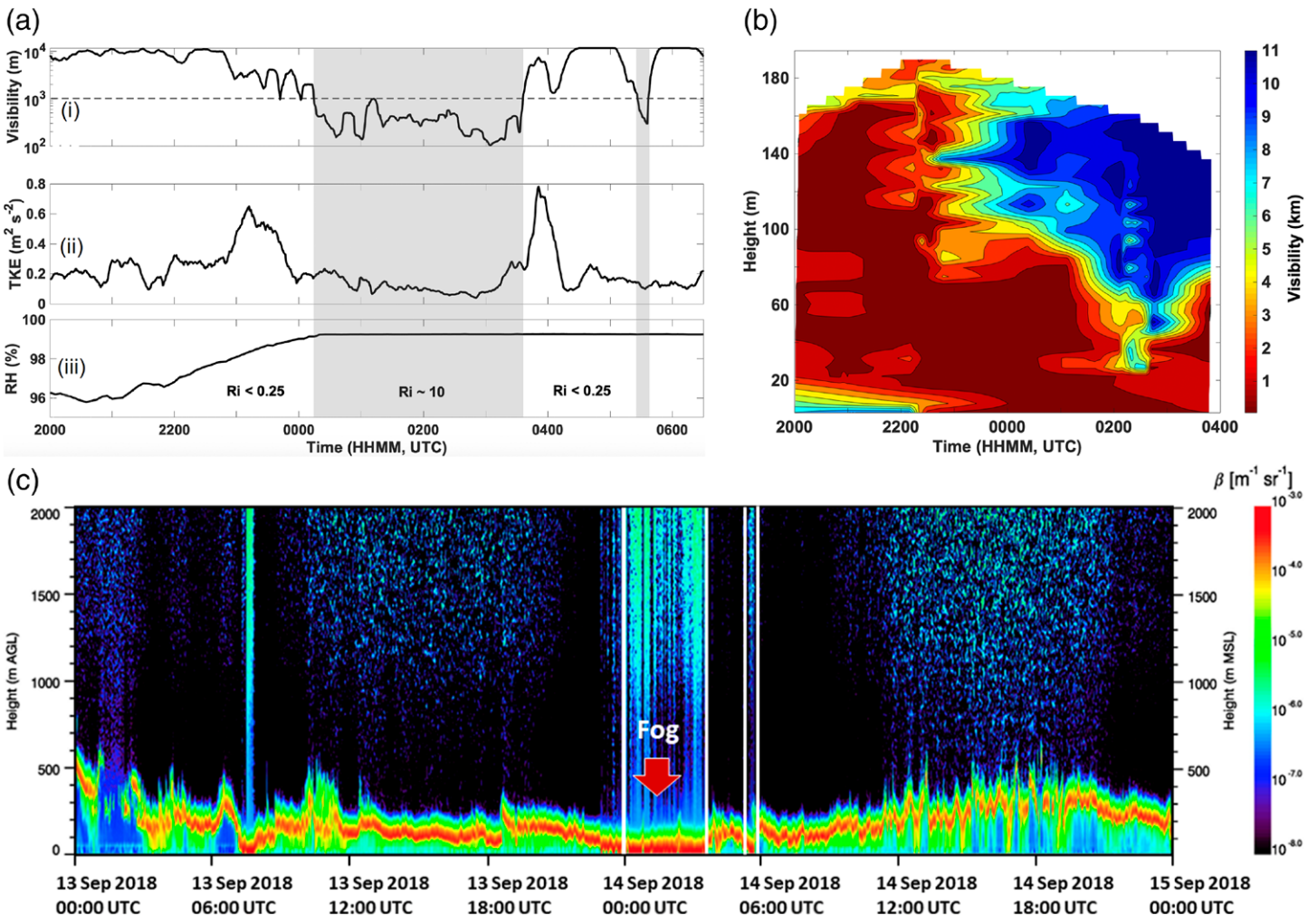


**Fig. 10. (a) Time series of near-surface (i) 5-min-averaged visibility by PWD, (ii) TKE, and (iii) RH at the Blackhead site from 2000 UTC 13 Sep to ~0630 UTC 14 Sep. (b) Contour plot of visibility with time (2000 UTC 13 Sep to 0400 UTC 14 Sep) from the surface to 200 m AGL, showing stratus lowering, development of fog near the surface, and penetration of clear air from above down near the surface. Visibility here was derived using the correlations between an optical particle counter suspended on the tethered balloon and a PWD. (c) Ceilometer backscatter for Blackhead.**

time evolution of the vertical profiles of visibility calculated using WRF with 1 km grid resolution and NSSL microphysics is shown in Fig. 11a, where three visibility algorithms (FSL, CVIS, and G2009) were employed. Their predictions varied, and G2009 exhibited the best agreement with data along the coastline with regard to $N_c$, LWC, and hence visibility. All algorithms captured a higher visibility layer underneath the stratus starting at ~2200 UTC, but with a larger fog layer thickness (~200 m) than in observations (~80 m). The timing of model fog appearance (~2230 UTC 13 September) and the onset of stratus rising (~0300 UTC 14 September) were in general agreement with observations (0000 and 0330UTC; Fig. 10). While observed fog reappearance (0520 UTC) was in good agreement with the model (0500 UTC), the longevity of the modeled fog was much longer (2 h) than in observations (20 min) (Figs. 10a,c and 11a). The 10 m wind velocity, SST, and visibility predicted by WRF for three representative instances are in Figs. 11b and 11c showing broad agreement with observations, although sensitivity to the parameterization scheme used is clear. Notwithstanding good near-surface predictions, WRF did not capture the observed vertical distribution of fog well, instead predicting a more intense and vertically extended fog layer. By using a large number (99) of vertical levels and activating the ocean mixed-layer option of WRF, fog predictions could be improved over more homogeneous areas (e.g., ocean; not shown). Given that turbulent transport and microphysical phenomena in inhomogeneous coastal terrain are predisposed for microscales, mesoscale models encounter difficulties in accurately capturing coastal fog in specific localities of heterogeneous terrain.

***COAMPS modeling.*** COAMPS was both a workhorse for calling out IOPs and a tool for post facto process studies and identification of NWP model deficiencies. One of the most interesting case studies came at the very end of the field campaign, during the night after IOP12, early on 5 October, whence a cold front over the Canadian Maritimes and NL trailed a deepening low over northern Quebec (see Figs. ES3 and ES4), generating strong (>15 m $s^{-1}$) model S/SE winds at 10 m MSL over the Labrador Strait. Roughly 2000 km south of NL, Tropical Cyclone (TC) Leslie (a category 1 hurricane on 2 October), was moving slowly northward. A strong high over the central North Atlantic bounded the region to the east. During multiple successive forecast runs, earliest with the 1200 UTC 3 October initialization, COAMPS predicted continuous fog on the morning of 5 October at all major C-FOG field sites, which was unusual for the campaign (Fig. 12a). The last forecast before the period of interest, initialized at 0000 UTC 5 October, reconfirmed fog from 0500 through 1000 UTC at all field sites, with the potential for local continuation around Ferryland through 1200 UTC. These predictions prompted a call for an unofficial IOP to capture potential details. However, with the exception of few ephemeral fog appearances, no fog was recorded on 5 October at any of the NL field sites (e.g., Fig. 12b), which led to a post-campaign analysis of the model behavior.

The model predicted a low-level stratus over Avalon Peninsula and surrounding waters at ~0000 UTC 5 October, with CBH steadily lowering in time. The cloud first appeared as fog over the highest elevations on Avalon (~260 m MSL) around 0100 UTC 5 October, and then engulfed lower elevations as the cloud base descended. Southerly winds ~8 m $s^{-1}$ were typical in the littoral zone south of Avalon, which advected fog over short distances off of the northern coastline. By 0700 UTC, the model CBH was very near the sea surface. Widely scattered precipitation starting ~0800 UTC yielded isolated "gaps" in fog coverage by temporarily increasing visibility. Additional gaps began to form starting at 1200 UTC over the northeast corners of Avalon, downwind of the longest overland fetches, concurrent with a rapid surface warming over land (Fig. 12a). This occurs in conjunction with a weakening of onshore flow (now S/SE) due to interaction between tropical cyclone Leslie and the extratropical system (Figs. ES3 and ES4). The result of this weakened cloud advection was the gradual retreat of fog from northeast to southwest over Avalon during the afternoon ahead of a late-day frontal passage.

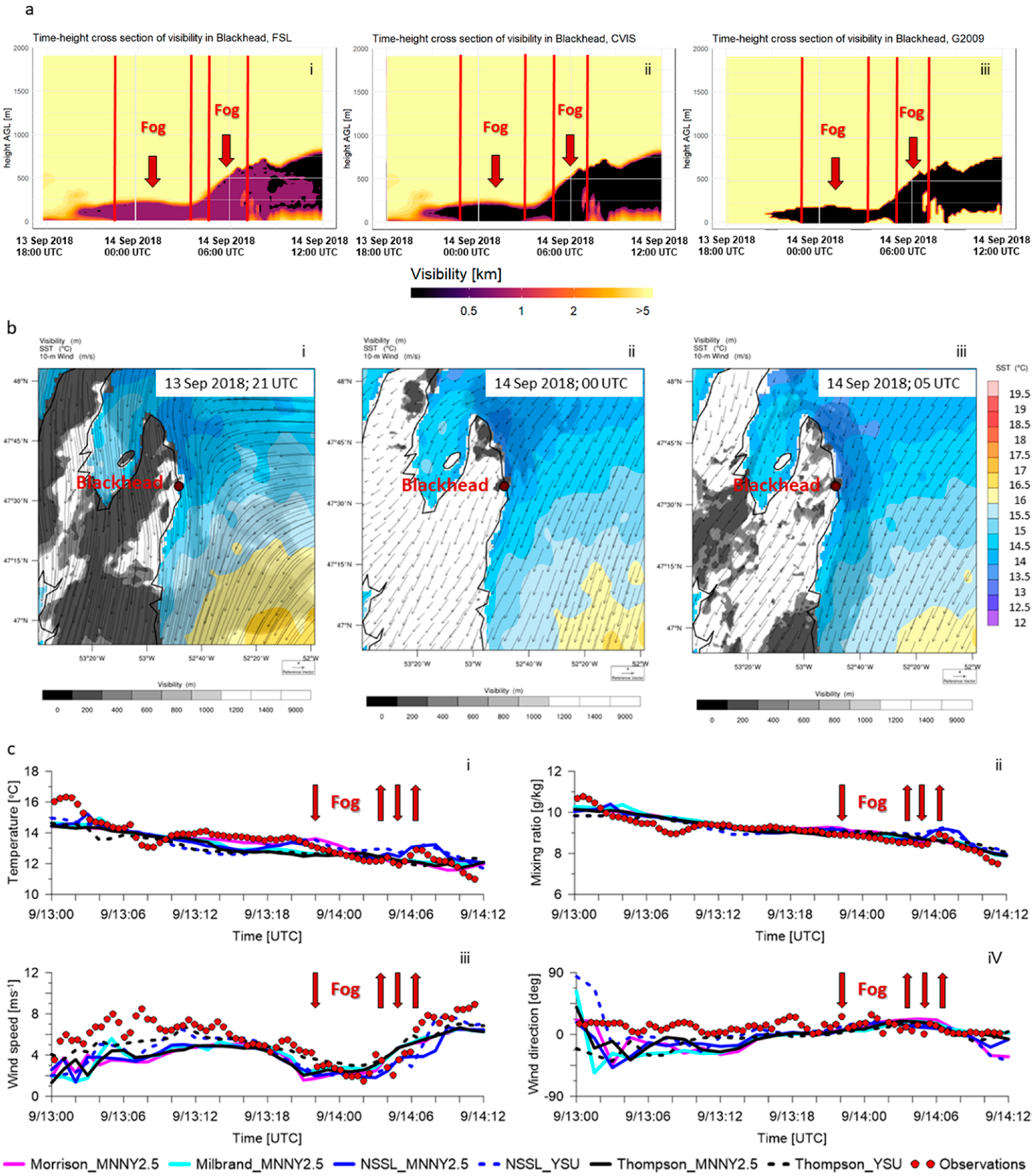


**Fig. 11. (a) Vertical WRF (with NSSL-2 microphysics) cross sections covering the onset, intensification, and dissipation of fog. Visibility algorithms used included (i) FSL (NOAA Forecast Systems Laboratory; Doran et al. 1999), (ii) CVIS [Bang et al. 2009; this combines FSL and Stoelinga and Warner (1999; SW99) algorithms], and (iii) G2009 (Gultepe et al. 2009). (b) 10 m wind velocity, SST, and fog (Vis < 1 km; in gray) for three selected times corresponding to conditions (i) that preceded fog formation, (ii) at fog onset, and (iii) at fog dissipation. (c) Near-surface 30-min-averaged observed (hydro-) meteorological parameters compared with simulations for Blackhead. Morrison et al. (2005, 2009), NSSL (Mansell et al. 2010), Milbrandt et al. (2010), and Thompson et al. (2008) microphysical schemes are used with YSU (Hong et al. 2006) and MYNN2.5 (Nakanishi and Niino 2006) PBL schemes. Downward arrows represents fog appearance and vice versa.**

With regard to observations, ceilometers at all major sites revealed a developing and lowering cloud base early on 5 October, broadly consistent with the model. The observed CBH lowered to only around 100 m MSL at Ferryland (Fig. 12b) and Blackhead, and to around 200 m MSL at Flatrock (not shown). Ferryland, however, underwent momentary fog episodes (visibility fluctuations in Fig. 12c), perhaps due to downward moisture entrainment from low clouds. Between 0000 and 0230 UTC, observations show that winds were gusty (~5–10 m $s^{-1}$), northerly (in contrast to model S/SE), humid (RH > 90%), rainy/drizzly and turbulent (Fig. 12c), but thereafter remained ~10 m $s^{-1}$, nearly saturated, and gradually turned S/SE while visibility remained clear. While the model CBH increased later in the morning, yielding persistent low cloud but no fog, the observed low cloud conditions dissipated soon after 1200 UTC at all sites with the passage of rain showers (Fig. 12c). A subsequent but temporary renewal of low cloud was seen at all sites in the afternoon (around 1500 UTC), which was not captured by the model. In all, COAMPS correctly predicted the presence, timing, and lowering of sustained

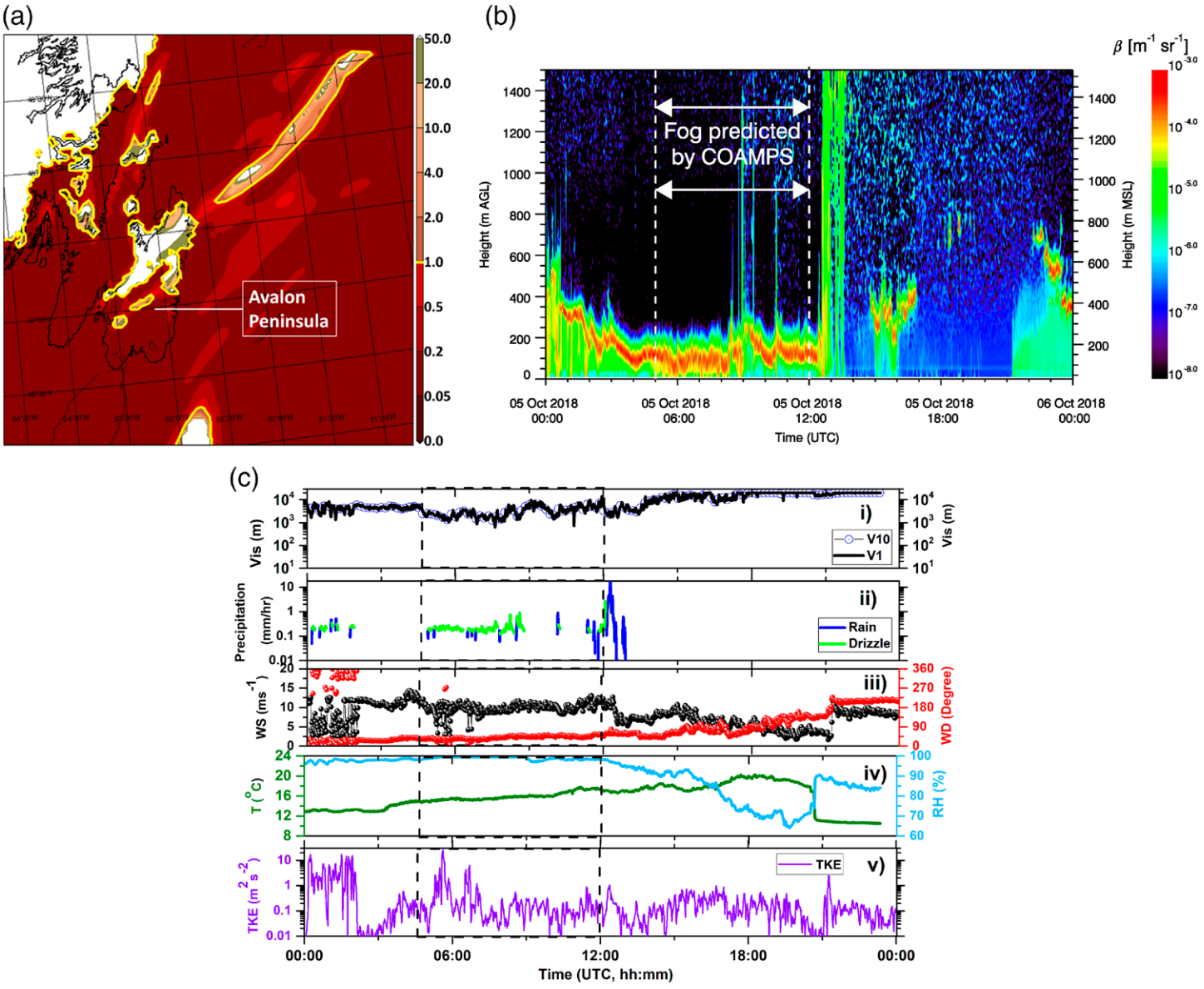


**Fig. 12. (a) COAMPS forecast of visibility (filled contours at 0.05, 0.2, 0.5, 1.0, 2.0, 4.0, 10, 20, and 50 km, thick black contour of 1 km visibility delineates fog) at 1200 UTC 5 Oct on a 2 km grid. (b) Backscatter ($\beta$) profile vs time for 5 Oct from a ceilometer at the Downs site. The period corresponding to fog predicted by COAMPS is indicated by the vertical dashed lines. (c) Visibility (10- and 1-min-averaged, $V_{10}$ and $V_1$) and 1-min-averaged precipitation from PWD, and meteorological parameters and TKE using 15 m sonic and *T*/RH (1-min-averaged) at the Downs 15 m flux tower on 5 Oct.**

overnight large-scale stratus, but incorrectly extended the base to the surface at least in some observational locations. This clearly demonstrates the need for the model to precisely capture detailed microscale physical processes. While subsidence and vertical mixing (entrainment) in this case are prima facie deficiencies of the model, contributions of other model elements such as microphysical parameterizations and vertical grid discretization cannot be discounted because of their interdependence, and work toward addressing them is being pursued.

***High-resolution simulations.*** High-resolution LES was integral to C-FOG process studies, and was directed at investigating the sensitivity of fog to several physical and microphysical factors ($N_c$, turbulent mixing, $\Delta_{a-s}$). LES allows resolving and hence in-depth numerical studies of microscale turbulent motions with grid spacing below 5 m, and C-FOG was aimed at extending previous LES studies on continental fog (e.g., Nakanishi and Niino 2006; Bergot 2013; Boutle et al. 2018; Mazoyer et al. 2017; Maronga and Bosveld 2017) to coastal fog cases. Some key differences between the two fog types are the abundance of moisture, complexity of terrain, characteristics and concentration of FCNs, and intrinsic advective processes such as the sea–land breeze in coastal areas.

Sensitivity studies were first conducted for a simplified marine (cold) fog case (full details can be found in Wainwright and Richter 2021). The simulations employed the LES mode of Cloud Model 1 version 19.6 (CM1; Bryan and Morrison 2012), which is a nonhydrostatic model designed for use in idealized studies of atmospheric phenomena; for details, see the "Numerical modeling overview" section in the supplemental material. A fixed-$N_c$ microphysical parameterization scheme was selected for the initial studies to emulate microphysics schemes of operational NWPs; simulations were performed varying $N_c$ across a range values typically applied in marine settings (50–150 cm$^{-3}$).

The initial fog formation and subsequent development (e.g., Fig. 13) were highly sensitive to $N_c$, as changes to $r_e$ alter longwave radiative cooling via impacts on the optical depth as well

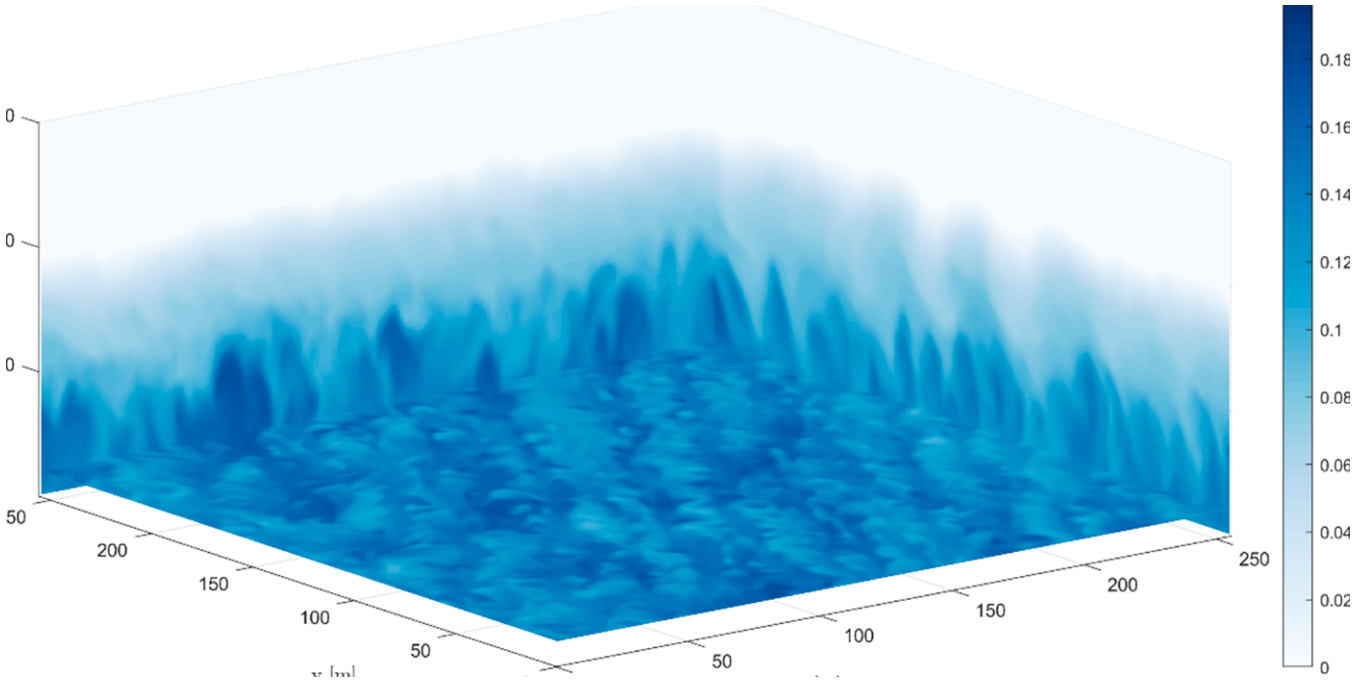


**Fig. 13. Instantaneous contours of LWC from LES of an idealized fog case at 2 m height and at the lateral boundaries after 9 h of simulation time. The simulations were initiated using an idealized warm fog setup with SST = 282 K, $T_a$ = 284 K ($\Delta_{a-s}$ = 2 K), $N_c$ = 100 cm$^{-3}$, and wind speed 2 m s$^{-1}$. The level of turbulent mixing was varied in the simulations by altering the wind speed, and across the simulations the wind speed was varied between 1 and 4 m s$^{-1}$. In the overall simulation program, initial $N_c$ was varied between 50 and 150 cm$^{-3}$ and $\Delta_{a-s}$ between 1 and 4 K.**

as droplet sedimentation via activated aerosols (Boutle et al. 2018). Turbulent mixing had a complex and nonlinear effect on the fog development (cf., Maronga and Bosveld 2017), and the effect of mixing was highly sensitive to the initial profile. Enhanced mixing increased the fog growth through the moist layer, but also hastened dissipation (broadly consistent with observations, cf., Fig. 10a) by enhancing entrainment of dry air from above. An increase of $\Delta_{a-s}$ yielded a stronger fog, which impacted the rest of the life cycle. The dependence of the three parameters tested was found to be nonlinear, given complex interactions among physical, radiative, and microphysical processes.

## Epilogue

C-FOG is a comprehensive multidisciplinary project designed to improve scientific understanding and predictability of the life cycle of coastal fog by observing physicochemical, dynamical, microphysical, thermodynamic, and environmental drivers over a range of space–time scales. A stunning array of measurement platforms was deployed over coastal land and ocean for approximately 1 month, collecting an extensive dataset that is available for the scientific community at large. This paper presented an overview of the field campaign and selected examples of resulting fundamental and numerical modeling studies that help identify mechanisms underlying fog life cycle as well as roadblocks for accurate fog forecasting.

Twelve land-based and three ship-based IOPs were conducted. Although the IOPs were called upon by experienced weather agency forecasters as well as academic researchers, the predictability of fog during C-FOG was ~50%. This low predictive skill can be largely attributed to space–time scale complexity contributed by land–atmosphere–ocean interactions, wherein smaller (micrometeorological and microphysical) scales play a decisive role. Microscales are not resolved by NWPs nor are they well captured by conventional observing systems. Thus, fog forecasting heavily relies on parameterizations (currently with large uncertainties), artificial intelligence techniques or local operational knowledge. It is our hope that fundamental knowledge gained by C-FOG will help address factors that stymie reliable fog forecasting.

A major finding is that large (synoptic)-scale weather systems alone are not good prognosticators of fog genesis and evolution, but the details of smaller (meso, micrometeorological, and microphysical) scales generated via scale interactions and aerosol dynamics play a crucial role and should be considered in fog modeling endeavors. The multipronged approach employed in C-FOG clearly demonstrates that resolvable (larger) scale motions are much better predicted by NWP models than fog, with life cycle of fog is sensitively determined by details of microscale (surface) processes within the ABL, including turbulence, entrainment, mixing, nucleation, condensation and evaporation, and autoconversion. Parameters that determine such processes, preferably universal (dimensionless) parameters, need to be identified and implemented in NWP models. In addition, C-FOG adumbrated the possibility of air–sea interaction thresholds that define conditions where upper-ocean plays a significant role in coastal fog life cycle by ways of air–sea fluxes, SST, ocean upwelling, and FCN injection (Mason et al. 1957). It also stressed the need for improved understanding of fog-microphysical processes as well as spatial (especially vertical) variation of microphysical parameters of ABL, measurements of which are virtually nonexistent. This is an aspect that conspicuously lags the progress of its cloud-microphysical counterpart (e.g., Grabowski et al. 2019; Gettelman et al. 2019). While current fog microphysical parameterizations are hinged on developments in cloud microphysics, which is a prudent first step, it appears that great strides in fog modeling are possible by understanding, quantifying and implementing in NWP models how intrinsic (coastal/marine/terrestrial) ABL attributes such as surface dynamical processes (e.g., fluxes, shear, stratification, stability, topographic), physicochemical characteristics (e.g., FCN sources, composition, transport,

transformations), thermodynamics (e.g., convection, radiation, phase changes), diel cycle, and their spatiotemporal variability determine the life of coastal fog.

**Acknowledgments.** This research was funded by ONR Grant N00014-18-1-2472 as a Multidisciplinary Initiative (see sidebar). We thank the initiative, commitment and guidance of ONR Program Officer Daniel Eleuterio and Assistant Program Officers Katherine Mulreany and Joshua Cossuth. We are grateful to C-FOG advisory committee members Walter Dabberdt, Andrew Heymsfield, and Jeffrey Reid for their expert advice. The invaluable logistical support of Mr. Marvin Willis of JonBoy Meteorological Services and Major Norm Scantland of Canadian DND and the assistance of the crew of R/V *Hugh R. Sharp* are gratefully acknowledged. The Pacific Northwest National Laboratory is operated by Battelle Memorial Institute for the DOE under Contract DE-AC05-76 RL01830

## References


Anderson, J. B., 1931: Observations from airplanes of cloud and fog conditions along the southern California coast. *Mon. Wea. Rev.*, **59**, 264–270, https://doi.org/10.1175/1520-0493(1931)59<264:OFAOCA>2.0.CO;2.

Ångström, A., 1920: Applications of heat radiation measurements to problems of the evaporation from lakes and heat convection at their surfaces. *Geogr. Ann.*, **2**, 237–252, https://doi.org/10.1080/20014422.1920.11880772.

Bang, C. H., J. W. Lee, and S. Y. Hong, 2009: Predictability experiments of fog and visibility in local airports over Korea using the WRF model. *J. Korean Soc. Atmos. Environ.*, **24**, 92–101.

Batchelor, G. K., 1959: Small-scale variation of convected quantities like temperature in turbulent fluid Part I. General discussion and the case of small conductivity. *J. Fluid Mech.*, **5**, 113–133, https://doi.org/10.1017/S002211205900009X.

Bergot, T., 2013: Small-scale structure of radiation fog: A large-eddy simulation study. *Quart. J. Roy. Meteor. Soc.*, **139**, 1099–1112, https://doi.org/10.1002/qj.2051.

Boutle, I., J. Price, I. Kudzotsa, H. Kokkola, and S. Romakkaniemi, 2018: Aerosol–fog interaction and the transition to well-mixed radiation fog. *Atmos. Chem. Phys.*, **18**, 7827–7840, https://doi.org/10.5194/acp-18-7827-2018.

Bowen, I. S., 1926: The ratio of heat losses by conduction and evaporation from water surfaces. *Phys. Rev.*, **27**, 779–787, https://doi.org/10.1103/PhysRev.27.779.

Bryan, G. H., and H. Morrison, 2012: Sensitivity of a simulated squall line to horizontal resolution and parameterization of microphysics. *Mon. Wea. Rev.*, **140**, 202–225, https://doi.org/10.1175/MWR-D-11-00046.1.

Daniels, Z. D., 2019: Quantifying HEL weapon system performance in a coastal fog environment. M.S. thesis, Meteorology Department, Naval Postgraduate School, 59 pp.

Deardorff, J. W., 1980: Cloud top entrainment instability. *J. Atmos. Sci.*, **37**, 131–147, https://doi.org/10.1175/1520-0469(1980)037<0131:CTEI>2.0.CO;2.

Doran, J. A., and Coauthors, 1999: The MM5 at the Air Force Weather Agency—New products to support military operations. *Eighth Conf. on Aviation, Range, and Aerospace Meteorology*, Dallas, TX, Amer. Meteor. Soc., 4.17, https://ams.confex.com/ams/99annual/abstracts/1125.htm.

Dorman, C. E., J. Mejia, D. Koračin, and D. McEvoy, 2017: Worldwide marine fog occurrence and climatology. *Marine Fog Challenges and Advancements in Observations, Modeling, and Forecasting*, D. Koračin and C. E. Dorman, Eds., Springer, 7–152.

——, ——, ——, and ——, 2020: World marine fog analysis based on 58-years of ship observations. *Int. J. Climatol.*, **40**, 145–168, https://doi.org/10.1002/joc.6200.

——, S.W. Hoch, I. Gultepe, H.J.S. Fernando, and R. Krishnamurthy, 2021: Large scale synoptic systems and fog during the C-FOG field experiment. *Bound. Layer Meteor.*, in press.

Fernando, H. J. S., 1991: Turbulent mixing in stratified fluids. *Annu. Rev. Fluid Mech.*, **23**, 455–493, https://doi.org/10.1146/annurev.fl.23.010191.002323.

——, and J. C. R. Hunt, 1997: Turbulence, waves and mixing at shear-free density interfaces. Part I. A theoretical model. *J. Fluid Mech.*, **347**, 197–234, https://doi.org/10.1017/S0022112097006514.

Fiorino, S. T., J. E. Bills, B. J. Elmore, S. R. Bose-Pillai, J. E. Schmidt, and K. J. Keefer, 2019: Assessing free-space optical communications through 4D weather cubes. *2019 IEEE Aerospace Conf.*, Big Sky, Montana, IEEE, 1–12, https://doi.org/10.1109/AERO.2019.8741941.

Gettelman, A., H. Morrison, and G. Thompson, 2019: Cloud microphysics across scales for weather and climate. *Current Trends in the Representation of Physical Processes in Weather and Climate Models*, D. A. Randall et al., Eds., Springer, 71–94.

Ghude, S. D., and Coauthors, 2017: Winter fog experiment over the Indo-Gangetic plains of India. *Current Sci.*, **112**,767–784, https://doi.org/10.18520/cs/v112/i04/767-784.

Grabowski, W. W., H. Morrison, S. I. Shima, G. C. Abade, P. Dziekan, and H. Pawlowska, 2019: Modeling of cloud microphysics: Can we do better? *Bull. Amer. Meteor. Soc.*, **100**, 655–672, https://doi.org/10.1175/BAMS-D-18-0005.1.

Grachev, A. A., L. S. Leo, H. J. S. Fernando, and C. W. Fairall, E. Creegan, B. W. Blomquist, A. J. Christman, and C. M. Hocut, 2018: Air-sea/land interaction in the coastal zone. *Bound.-Layer Meteor.*, **167**, 181–210, https://doi.org/10.1007/s10546-017-0326-2.

Gultepe, I., and Coauthors, 2007: Fog research: A review of past achievements and future perspectives. *Pure Appl. Geophys.*, **164**, 1121–1159, https://doi.org/10.1007/s00024-007-0211-x.

——, and Coauthors, 2009: The fog remote sensing and modeling field project. *Bull. Amer. Meteor. Soc.*, **90**, 341–360, https://doi.org/10.1175/2008BAMS2354.1.

——, and Coauthors, 2014: Ice fog in Arctic during FRAM–Ice Fog project: Aviation and nowcasting applications. *Bull. Amer. Meteor. Soc.*, **95**, 211–226, https://doi.org/10.1175/BAMS-D-11-00071.1.

——, and Coauthors, 2015: A review on ice fog measurements and modeling. *Atmos. Res.*, **151**, 2–19, https://doi.org/10.1016/j.atmosres.2014.04.014.

——, and Coauthors, 2016: An overview of the MATERHORN fog project: Observations and predictability. *Pure Appl. Geophys.*, **173**, 2983–3010, https://doi.org/10.1007/s00024-016-1374-0.

——, and J. A. Milbrandt, and B. Zhou, 2017: Marine fog: A review on microphysics and visibility prediction. *Marine Fog: Challenges and Advancements in Observations, Modeling, and Forecasting*, D. Koracin and C. Dorman, Eds., Springer, 345–394.

Gurka, J. J., 1978: The role of inward mixing in the dissipation of fog and stratus. *Mon. Wea. Rev.*, **106**, 1633–1635, https://doi.org/10.1175/1520-0493(1978)106<1633:TROIMI>2.0.CO;2.

Haeffelin, M., T. Bergot, T. Elias, R. Tardif, D. Carrer, P. Chazette, and L. Gomes, 2010: PARISFOG: Shedding new light on fog physical processes. *Bull. Amer. Meteor. Soc.*, **91**, 767–783, https://doi.org/10.1175/2009BAMS2671.1.

Hong, S. Y., Y. Noh, and J. Dudhia, 2006: A new vertical diffusion package with an explicit treatment of entrainment processes. *Mon. Wea. Rev.*, **134**, 2318–2341, https://doi.org/10.1175/MWR3199.1.

Hudson, J. G., 1980: Relationship between fog condensation nuclei and fog microstructure. *J. Atmos. Sci.*, **37**, 1854–1867, https://doi.org/10.1175/1520-0469(1980)037<1854:RBFCNA>2.0.CO;2.

Isaac, G. A., T. Bullock, J. Beale, and S. Beale, 2020: Characterizing and predicting marine fog offshore Newfoundland and Labrador. *Wea. Forecasting*, **35**, 347–365, https://doi.org/10.1175/WAF-D-19-0085.1.

Jeffreys, H., 1918: Some problems of evaporation. *Philos. Mag.*, **35**, 270–280, https://doi.org/10.1080/14786440308635761.

Kim, C. K., M. Stuefer, C. G. Schmitt, A. Heymsfield, and G. Thompson, 2014: Numerical modeling of ice fog in interior Alaska using the weather research and forecasting model. *Pure Appl. Geophys.*, **171**, 1963–1982, https://doi.org/10.1007/s00024-013-0766-7.

Koračin, D., J. Lewis, W. T. Thompson, C. E. Dorman, and J. A. Businger, 2001: Transition of stratus into fog along the California coast: Observations and modeling. *J. Atmos. Sci.*, **58**, 1714–1731, https://doi.org/10.1175/1520-0469(2001)058<1714:TOSIFA>2.0.CO;2.

——, J. A. Businger, C. E. Dorman, and J. M. Lewis, 2005: Formation, evolution, and dissipation of coastal sea fog. *Bound.-Layer Meteor.*, **117**, 447–478, https://doi.org/10.1007/s10546-005-2772-5.

——, C. E. Dorman, J. M. Lewis, J. G. Hudson, E. M. Wilcox, and A. Torregrosa, 2014: Marine fog: A review. *Atmos. Res.*, **143**, 142–175, https://doi.org/10.1016/j.atmosres.2013.12.012.

Leipper, D. F., 1948: Fog development at San Diego, California. *J. Mar. Res.*, **VII**, 337–346.

——, 1994: Fog on the U.S. West Coast: A review. *Bull. Amer. Meteor. Soc.*, **75**, 229–240, https://doi.org/10.1175/1520-0477(1994)075<0229:FOTUWC>2.0.CO;2.

Li, P., G. Fu, and C. Lu, 2012: Large-scale environmental influences on the onset, maintenance, and dissipation of six sea fog cases over the Yellow Sea. *Pure Appl. Geophys.*, **169**, 983–1000, https://doi.org/10.1007/s00024-011-0348-5.

Lin, C. Y., Z. Zhang, Z. Pu, and F. Wang, 2017: Numerical simulations of an advection fog event over Shanghai Pudong International Airport with the WRF model. *J. Meteor. Res.*, **31**, 874–889, https://doi.org/10.1007/s13351-017-6187-2.

Liu, D. Y., W. L. Yan, J. Yang, M. J. Pu, S. J. Niu, and Z. H. Li, 2016: A study of the physical processes of an advection fog boundary layer. *Bound.-Layer Meteor.*, **158**, 125–138, https://doi.org/10.1007/s10546-015-0076-y.

Lozovatsky, I., C. Wainwright, E. Creegan, and H. J. S. Fernando, 2021: Ocean turbulence and mixing near the shelf break south-east of Nova Scotia. *Bound.-Layer Meteor.*, https://doi.org/10.1007/s10546-020-00576-z, in press.

Mansell, E. R., C. L. Ziegler, and E. C. Bruning, 2010: Simulated electrification of a small thunderstorm with two-moment bulk microphysics. *J. Atmos. Sci.*, **67**, 171–194, https://doi.org/10.1175/2009JAS2965.1.

Maronga, B., and F. C. Bosveld, 2017: Key parameters for the life cycle of nocturnal radiation fog: A comprehensive large-eddy simulation study. *Quart. J. Roy. Meteor. Soc.*, **143**, 2463–2480, https://doi.org/10.1002/qj.3100.

Mason, B. J., 1957: The oceans as source of cloud-forming nuclei. *Geofis. Pura Appl.*, **36**, 148–155, https://doi.org/10.1007/BF01993002.

Mazoyer, M., C. Lac, O. Thouron, T. Bergot, V. Masson, and L. Musson-Genon, 2017: Large eddy simulation of radiation fog: Impact of dynamics on the fog life cycle. *Atmos. Chem. Phys.*, **17**, 13 017–13 035, https://doi.org/10.5194/acp-17-13017-2017.

McGraw, R., and Y. Liu, 2003: Kinetic potential and barrier crossing: A model for warm cloud drizzle formation. *Phys. Rev. Lett.*, **90**, 018501, https://doi.org/10.1103/PhysRevLett.90.018501.

Meyer, M. B., J. E. Jiusto, and G. G. Lala, 1980: Measurements of visual range and radiation-fog (Haze) microphysics. *J. Atmos. Sci.*, **37**, 622–629, https://doi.org/10.1175/1520-0469(1980)037<0622:MOVRAR>2.0.CO;2.

Michaelides, S. C., Ed., 2005: Short range forecasting methods of fog, visibility and low clouds: Workshop proceedings. Earth System Science and Environmental Management Final Rep. COST-722 Act, 130 pp.

Milbrandt, J. A., M. K. Yau, J. Mailhot, S. Bélair, and R. McTaggart-Cowan, 2010: Simulation of an orographic precipitation event during IMPROVE-2. Part II: Sensitivity to the number of moments in the bulk microphysics scheme. *Mon. Wea. Rev.*, **138**, 625–642, https://doi.org/10.1175/2009MWR3121.1.

Mori, S., and F. S. Marzano, 2015: Microphysical characterization of free space optical link due to hydrometeor and fog effects. *Appl. Opt.*, **54**, 6787–6803, https://doi.org/10.1364/AO.54.006787.

Morrison, H., J. A. Curry, and V. I. Khvorostyanov, 2005: A new double-moment microphysics parameterization for application in clouds and climate models. Part I: Description. *J. Atmos. Sci.*, **62**, 1665–1677, https://doi.org/10.1175/JAS3446.1.

——, G. Thompson, and V. Tatarskii, 2009: Impact of cloud microphysics on the development of trailing stratiform precipitation in a simulated squall line: Comparison of one- and two-moment schemes. *Mon. Wea. Rev.*, **137**, 991–1007, https://doi.org/10.1175/2008MWR2556.1.

Myers, J. N., 1968: Fog. *Sci. Amer.*, **219**, 74–82, https://doi.org/10.1038/scientificamerican1268-74.

Nakanishi, M., 2000: Large-eddy simulation of radiation fog. *Bound.-Layer Meteor.*, **94**, 461–493, https://doi.org/10.1023/A:1002490423389.

——, and H. Niino, 2006: An improved Mellor–Yamada level-3 model: Its numerical stability and application to a regional prediction of advection fog. *Bound.-Layer Meteor.*, **119**, 397–407, https://doi.org/10.1007/s10546-005-9030-8.

Noonkester, V. R., 1979: Coastal marine fog in Southern California. *Mon. Wea. Rev.*, **107**, 830–851, https://doi.org/10.1175/1520-0493(1979)107<0830:CMFISC>2.0.CO;2.

O'Brien, T. A., L. C. Sloan, P. Y. Chuang, I. C. Faloona, and J. A. Johnstone, 2013: Multidecadal simulation of coastal fog with a regional climate model. *Climate Dyn.*, **40**, 2801–2812, https://doi.org/10.1007/s00382-012-1486-x.

Pósfai, M., J. R. Anderson, P. R. Buseck, and H. Sievering, 1999: Soot and sulfate aerosol particles in the remote marine troposphere. *J. Geophys. Atmos.*, **104**, 21 685–21 693, https://doi.org/10.1029/1999JD900208.

Price, J. D., and Coauthors, 2018: LANFEX: A field and modeling study to improve our understanding and forecasting of radiation fog. *Bull. Amer. Meteor. Soc.*, **99**, 2061–2077, https://doi.org/10.1175/BAMS-D-16-0299.1.

Pu, Z., C. N. Chachere, S. W. Hoch, E. Pardyjak, and I. Gultepe, 2016: Numerical prediction of cold season fog events over complex terrain: The performance of the WRF model during MATERHORN-fog and early evaluation. *Pure Appl. Geophys.*, **173**, 3165–3186, https://doi.org/10.1007/s00024-016-1375-z.

Román-Cascón, C., G. J. Steeneveld, C. Yagüe, M. Sastre, J. A. Arrillaga, and G. Maqueda, 2016: Forecasting radiation fog at climatologically contrasting sites: Evaluation of statistical methods and WRF. *Quart. J. Roy. Meteor. Soc.*, **142**, 1048–1063, https://doi.org/10.1002/qj.2708.

Simei, X., B. Chenglan, J. Dezhong, and Z. Bin, 2001: Role of sea ice in air-sea exchange and its relation to sea fog. *Chinese J. Polar Sci.*, **12**, 119–132.

Simpson, J. E., 1999: *Gravity Currents: In the Environment and the Laboratory*. 2nd ed. Cambridge University Press, 260 pp.

Skamarock, W. C., and Coauthors, 2008: A description of the Advanced Research WRF version 3. NCAR Tech. Note NCAR/TN-475+STR, 113 pp., https://doi.org/10.5065/D68S4MVH.

Spirig, R., and Coauthors, 2019: Probing the fog life cycles in the Namib Desert. *Bull. Amer. Meteor. Soc.*, **100**, 2491–2507, https://doi.org/10.1175/BAMS-D-18-0142.1.

Steeneveld, G. J., R. J. Ronda, and A. A. M. Holtslag, 2015: The challenge of forecasting the onset and development of radiation fog using mesoscale atmospheric models. *Bound.-Layer Meteor.*, **154**, 265–289, https://doi.org/10.1007/s10546-014-9973-8.

Stoelinga, M. T., and T. T. Warner, 1999: Nonhydrostatic, mesobeta-scale model simulations of cloud ceiling and visibility for an East Coast winter precipitation event. *J. Appl. Meteor.*, **38**, 385–404, https://doi.org/10.1175/1520-0450(1999)038<0385:NMSMSO>2.0.CO;2.

Sverdrup, H. U., 1942: *Oceanography for Meteorologists*. Prentice-Hall, 246 pp.

Taylor, G. I., 1917: The formation of fog and mist. *Quart. J. Roy. Meteor. Soc.*, **43**, 241–268, https://doi.org/10.1002/qj.49704318302.

Thompson, G., and Coauthors, 2008: Explicit forecasts of winter precipitation using an improved bulk microphysics scheme. Part II: Implementation of a new snow parameterization. *Mon. Wea. Rev.*, **136**, 5095–5115, https://doi.org/10.1175/2008MWR2387.1.

Torregrosa, A., T. O'Brien, and I. Faloon, 2014: Coastal fog, climate change, and the environment. *Eos, Trans. Amer. Geophys. Union*, **95**, 473–474, https://doi.org/10.1002/2014EO500001.

Vasseur, H., and C. J. Gibbins, 1996: Inference of fog characteristics from attenuation measurements at millimeter and optical wavelengths. *Radio Sci.*, **31**, 1089–1097, https://doi.org/10.1029/96RS01725.

Wainwright, C., and D. Richter, 2021: Investigating the sensitivity of marine fog to physical and microphysical processes using large-eddy simulation. *Bound.-Layer Meteor.*, https://doi.org/10.1007/s10546-020-00599-6, in press.

Wilkinson, J. M., A. N. Porson, F. J. Bornemann, M. Weeks, P. R. Field, and A. P. Lock, 2013: Improved microphysical parametrization of drizzle and fog for operational forecasting using the Met Office Unified Model. *Quart. J. Roy. Meteor. Soc.*, **139**, 488–500, https://doi.org/10.1002/qj.1975.

WMO, 1992: International meteorological vocabulary. WMO-182, 784 pp.

Zhang, D., T. Sullivan, N. E. O'Connor, R. Gillespie, and F. Regan, 2015: Coastal fog detection using visual sensing. *OCEANS 2015*, Genoa, Italy, IEEE, 1–5, https://doi.org/10.1109/OCEANS-Genova.2015.7271683.

Zhang, S. P., S. P. Xie, Q. Y. Liu, Y. Q. Yang, X. G. Wang, and Z. P. Ren, 2009: Seasonal variations of Yellow Sea fog: Observations and mechanisms. *J. Climate*, **22**, 6758–6772, https://doi.org/10.1175/2009JCLI2806.1.